ALMA MATER STUDIORUM - UNIVERSITÀ DI BOLOGNA

Dottorato di Ricerca

in

Meccanica e scienze avanzate dell'ingegneria

Ciclo 31°

Settore Concorsuale di afferenza 09/A2 Settore

Settore Scientifico disciplinare ING-IND/13

A NEW OVERCONSTRAINED GOUGH-STEWART PLATFORM-BASED MANIPULATOR OPERATING UNDER FORCE CONTROL

Presentata da: **Luca Luzi**

Coordinatore Dottorato: Prof. **Marco Carricato**

Supervisore: Prof. **Vincenzo Parenti Castelli**

Esame Finale anno 2019

ABSTRACT

In vitro tests are essential to better understand the human joint behavior and to design more accurate prostheses and orthoses. In the literature, several test rigs have been presented that can be used to characterize the human joints for specific applications but poorly fit into the study when more general conditions are required. In 2014 the Group of Robotics, Automation and articular Biomechanics (GRAB) of the University of Bologna built an in vitro test rig that overcame these limitations. Even though the machine is capable to work with high accuracy, some improvements can be done in order to reduce the test time and simplify certain operations. Therefore, recently GRAB started the design of a new in vitro test rig, which can be regarded as an evolution of the previous one.

The test rig comprises a number of subsystems one of which is the loading system that represents the core of the machine. In particular, this work presents a new manipulator whose features make it suitable as loading system for the new test rig.

The new manipulator is an overconstrained Gough-Stewart platform-based robot. This property is useful since it makes it possible to realize a six degrees-of-freedom manipulator with a smaller number of joints and a higher stiffness with respect to a standard Gough-Stewart manipulator of the same size. Moreover, the manipulator does not require spherical joints and thrust journal bearings, thus allowing a larger workspace and simplifying the physical realization of the manipulator.

The geometrical characteristics of the manipulator are shown, and the kinematic analysis is presented. A solution for the position analysis is proposed and the Jacobin matrix is derived. Furthermore, a singularity and workspace numerical analyses are presented. The geometrical interpretation of the singularities is provided.

TABLE OF CONTENTS

CHAPTER 1 - INTRODUCTION

The knowledge of the behavior of the human joints is of great importance to develop proper models useful for prosthesis and orthosis design. In vitro experimental studies play a fundamental role in understanding the kinematic, kinetostatic and dynamic behaviors of human joints and in validating biomechanical models.

In the last thirty years several in vitro test rigs have been presented. They can be divided into two main groups (Fig. 1.1): the human joint simulators and the robot-based systems.

1. The human joint simulators (the most famous one being the Oxford Rig [1]) focus on the joint kinematics, trying to reproduce the physiological movements of the joints. In general, these devices move a limb with no loads or with only a limited actuation that can simulate only specific loading conditions.
2. The robot-based systems [2] are more focused on the kinetostatic analysis and aim at reproducing the loading conditions typical of daily tasks. These devices are generally composed of manipulators with several degrees of freedom (DOF) to apply the loads required during in vitro tests. Loads depend on the motion task to simulate. The scope of a standard test is generally measuring the relative motion between the bones of the joint, while applying a defined external load without introducing additional unwanted constraints on the bone relative motion. In other words, a test is performed in force control.

Current rigs have some typical limitations. Human joint simulators allow a large achievable flexion range, but very few loading conditions can be simulated. Vice versa, robot-based systems simulate several loading scenario, but the range of motion is very limited, due to the use of industrial robots in such applications.

In 2014 GRAB developed a new test rig [3]. According to the above-mentioned classification, it can be considered as a robot-based system and makes use of a six-DOF cable-driven parallel manipulator to load the joint. It showed both to fulfil the required accuracy and repeatability and to overcome the limitations of these devices. However, some aspects can be improved.

For the sake of clarity, a brief explanation of the GRAB robot-based system is given here. The system is composed of (Fig. 1.2): a frame (5), a loading system (6, 8) that provides the desired loads, and fixation systems connected to the rings (4, 6) that allows the

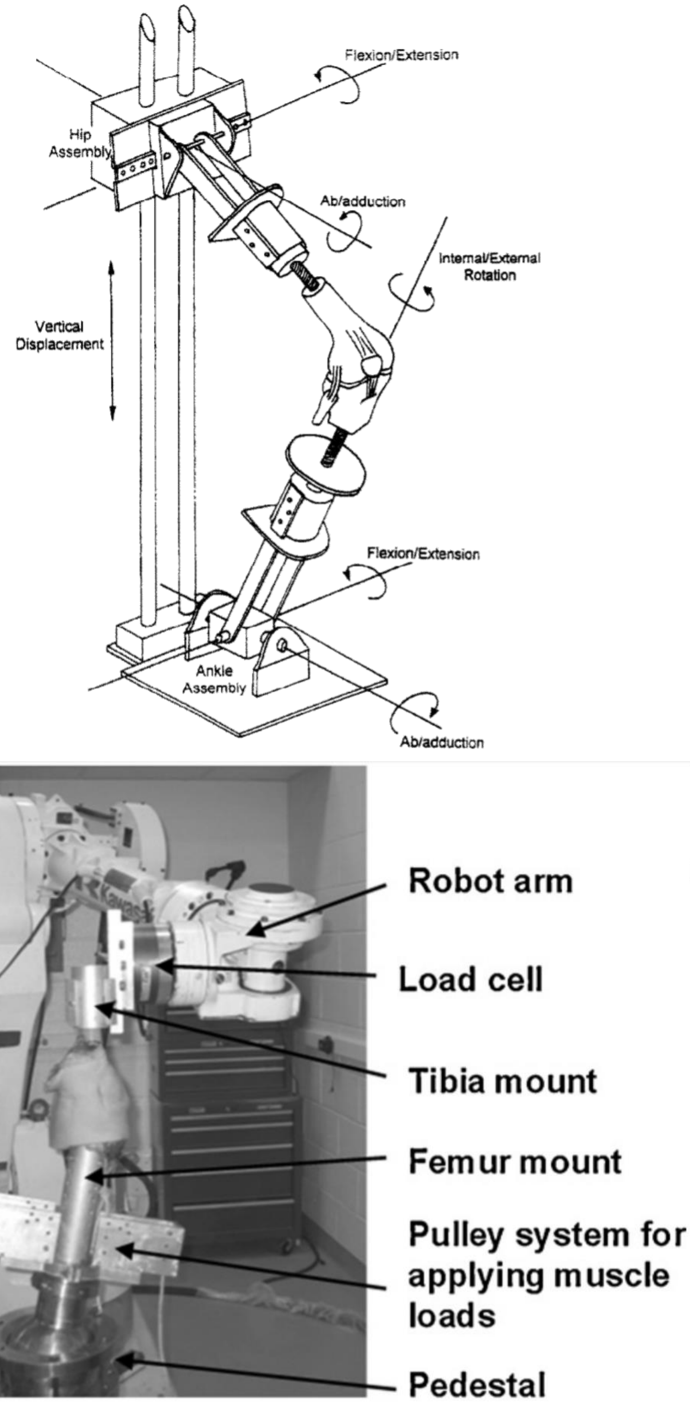

Figure 1.1. Test rigs: human joint simulator (upper figure); robot-based system (lower figure).

specimen to be properly mounted on the machine. The fixation systems are used to precisely and rigidly position the specimen (3, 10 in Fig. 1.2) with respect to the frame or other parts of the rig. In general, two fixation systems are used, one for the femur and the other for the tibia.

In [4], some improvements were introduced to the test rig. In particular, an exhaustive analysis is reported for the loading system (6, 8 in Fig. 1.2): the system that matched some load specifications at best was chosen among a series of different parallel manipulators. Indeed, parallel manipulators are known for their stiffness and for their relatively small dexterous workspace: these characteristics perfectly fit the loading system requirements. In particular, different types of Gough-Stewart (GS) platforms were compared in [4]. A GS platform comprises six serial chains (legs) of type SPU (where S, P, U stands for spherical, prismatic and universal joints respectively) connecting the movable platform to the base. GS platforms are frequently defined as m-n GS according to the numbers m and n of attaching points (i.e., the centers of the S and U joints) on the base and platform respectively. For instance, the most general GS platform is of type 6-6 and features six attachment points on both the base and the platform. In general, the P joints are actuated while the S and U joints are passive. As a result, the platform has six DOF with respect to the base that are controlled by the six active prismatic joints. In [4], the 6-6, 6-3, and a decoupled type GS platforms were compared in terms of workspace size, singularities within the workspace, maximum and minimum actuator forces needed to perform the same task, and design complexity: the decoupled platform did not match the workspace requirement, while the 6-3 and 6-6 GS platform had similar static behavior. Since the 6-3 GS platform required a higher design complexity, the 6-6 GS platform was initially chosen for the loading system.

At that stage of development, the dimension of the load cells required by the control system was not considered. Since the loading system must operate under high accuracy conditions, high precision but bulky load cells were chosen. Considering them on the workspace analysis, both the 6-6 and the 6-3 GS platform were no longer appropriate.

In this context, this thesis presents a new GS platform-based manipulator that provides relevant improvements with respect to the previous cable-driven loading system and to those analyzed in [4]. The new manipulator is a six-DOF overconstrained parallel manipulator, composed of a smaller number of kinematic pairs with respect to the manipulators previously considered. Moreover, a particular connection between the actuators and the mobile platform has been devised that makes it possible to mount high precision load cells, which require a large volume, but are essential for an accurate force control.

To show the novelty of the new manipulator with respect to similar existing ones, a state of the art about the different types of six-DOF GS platforms is presented. A complete state of the art on the general GS platform can be found in [5,6].

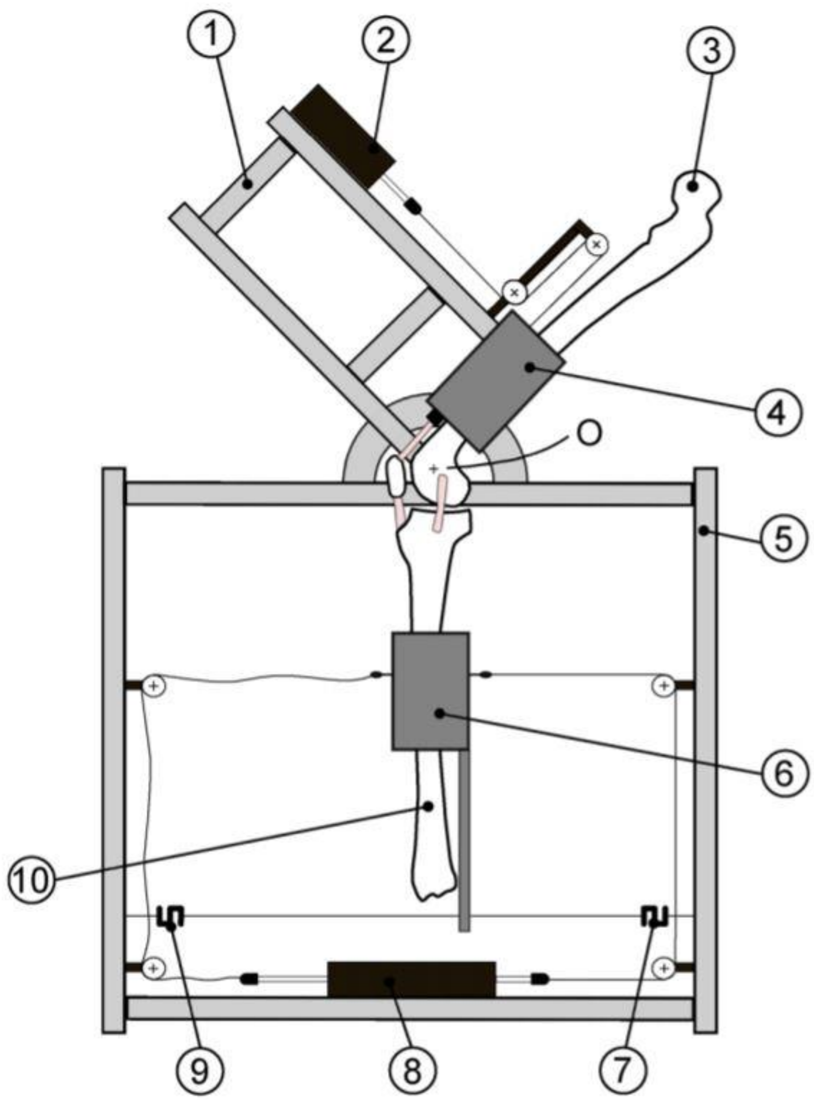

Figure 1.2. Test rig: two-dimensional representation.

State of the art

As described in [5], parallel manipulators have some advantages with respect to the serial ones. Firstly, the end-effector is less sensitive to errors of the actuated joints, ensuring high positioning accuracy. Moreover, they generally feature a high payload to manipulator-weight ratio, since the external loads acting on the movable platform are equilibrated by the various chains that connect the platform to the base.

The GS platform is the most popular six-DOF parallel robot and the above-mentioned advantages led to its large diffusion in industrial applications. In the literature, a significant number of manipulators based on the GS platform were presented and can be grouped according to several classifications, like the planar/spatial mechanism category, the number of degrees of freedom and the type of actuation. Since this work deals with a six-DOF mechanism, the following classification criteria are considered:

1. number of attachment points m and n of the leg actuators on the mobile platform and the fixed base;

2. type of kinematic chains that connect the mobile platform to the fixed base; e.g. UPS or other architectures.

The invention is attributed to Gough and Stewart, although Gough was the first proposing the platform as a mechanism in 1947, while in 1954-1955 he used the mechanism as a core of a tire-testing machine [7]. Only in 1965, Stewart proposed a similar platform [8] for a flight simulator and since then the mechanism was used for several applications, like:

1. machine tools;
2. flight simulators;
3. surgical precision devices;
4. vibration suppressors.

The Gough platform (Fig. 1.3) can be considered as the Standard GS platform. Indeed, the mechanism is composed of six cylindrical actuators, each one connected by means of spherical joints and universal joints to the mobile platform and to the fixed base respectively. The Stewart solution is a 6-3 GS platform and the legs are connected two by two as in Fig. 1.4. According to the classifications described above, the Gough Standard platform can be classified as a 6-6 GS platform with six UPS legs, whereas the Stewart platform as a 6-3 GS platform with three 2U2P2S legs.

One of the first evolution of the GS platform is the mechanism proposed in 1979 by McCallion and Truong [9]. This is a six-DOF work station with three 2U2H4R legs, where H stands for helicoidal pair. In this case, the connection of the legs with the mobile platform is a special joint composed of 4 revolute (R) joints that can be considered as a double spherical joint. The manipulator was proposed for assembly operations (Fig. 1.5-a) and proved to be rigid and accurate, light and maneuverable. The Stewart solution has a particular actuator arrangement so that only three out of six are connected to the mobile platform. Differently, the McCallion version has all six actuators connected in pairs to the mobile platform with a triangular arrangement of linkages (Fig. 1.5-b).

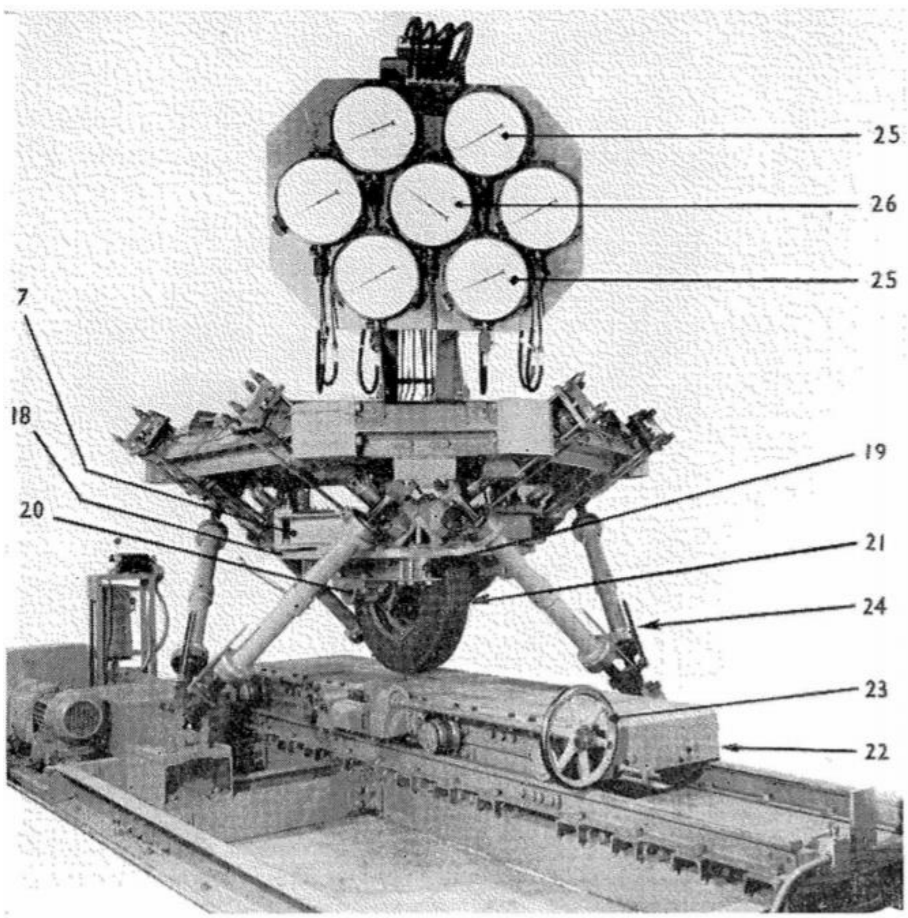

Figure 1.3. 6-6 GS platform designed by Gough [7].

Therefore, according to the second classification, the GS platform proposed by McCallion and Truong is very different from the Stewart one: it is worth noting that the forces that act on the actuators of the McCallion and Truong platform, as for the Gough platform, have direction along the P axis, thus being subjected by axial tensile stress. On the contrary, the Stewart platform actuators are subjected also to bending.

In 1983 Hunt [10] analyzed, via the screw theory, the kinematic structure (namely the

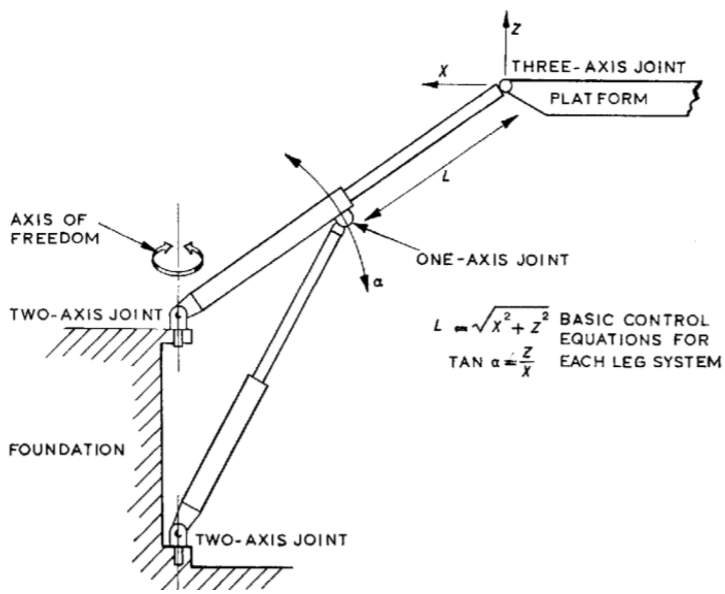

Figure 1.4. Connection of the legs to the mobile platform and to the fixed base of the Stewart platform [8].

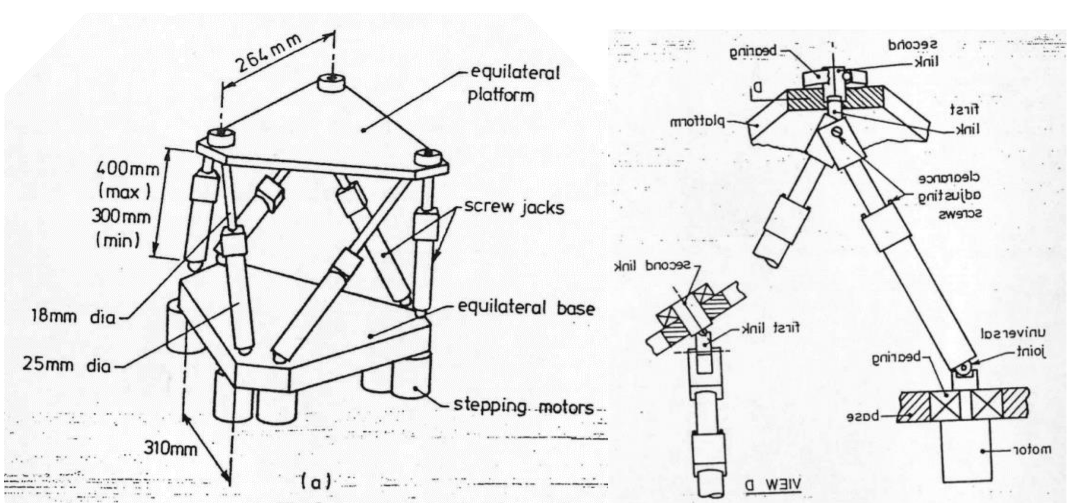

Figure 1.5. 6-3 GS platform designed by McCallion and Truong [9]: a) tridimensional representation of the manipulator; b) kinematic structure of each connection arrangement.

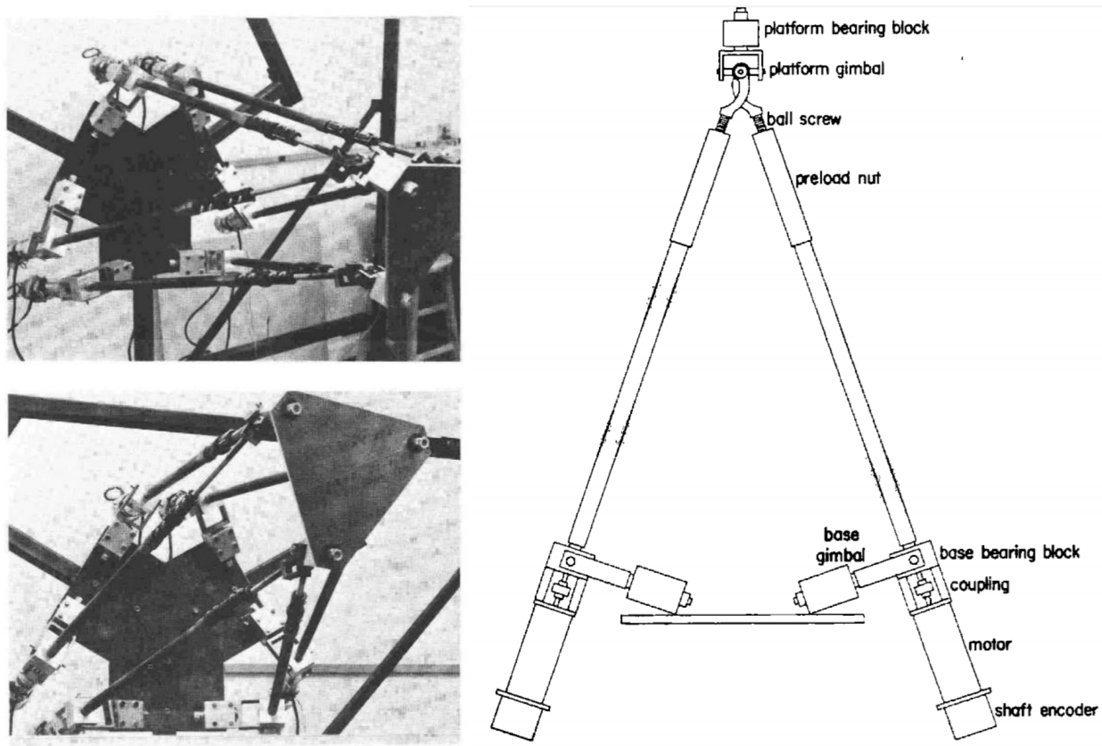

Figure 1.6. On the left, GS platform prototype built at Oregon State University [11]; on the right, linkage arrangement for the connection of the mobile platform with the fixed base.

links and kinematic pairs) of the existing parallel manipulators and provided general principles for the determination of more and more promising parallel architectures. This can be considered the starting point for the study of the workspace and singularities of the GS platform. In 1986 Fitcher [11] proposed the equations to solve the inverse position, velocity and static analyses of the general GS platform. Some singularity configurations for a 6-3 GS platform were shown and a workspace analysis was conducted. The results are confirmed by experimental analysis on the platform shown in Fig. 1.6. M. Raghavan [12] and C.W. Wampler [13] numerically showed that the direct position analysis (DPA) of the GS platform has 40 nonsingular solutions at most, considering both the real and complex ones, and M. L. Husty showed a method [14] that allows all 40 solutions of the DPA to be determined, obtained by a univariate polynomial of 40th degree. Dietmaier [15] showed that the 6-6 GS mechanism can have up to 40 real solutions. Innocenti and Parenti Castelli analytically solved the DPA first for the 4-4 GS platform [16], then for all the architectures of fully parallel mechanisms [17]. Only in 1998, Dietmaier [15]

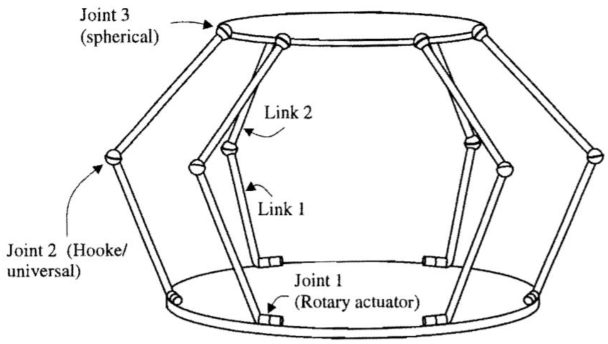

a)

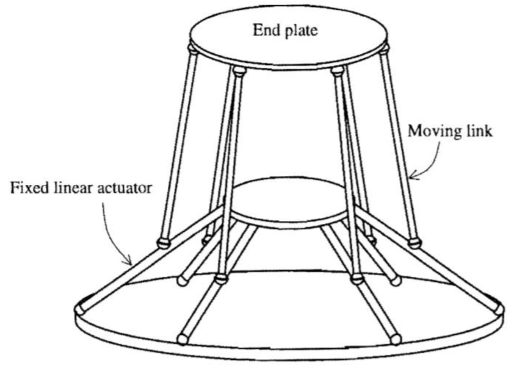

b)

Figure 1.7. Ari et al. GS platforms [18]: on the left, a 6-6 GS platform with six RUS legs; on the right, 6-6 GS platform with six PSS.

proposed a method to determine the geometrical parameters of a general GS platform which provides 40 real solutions of the DPA problem.

New versions of the GS platform were proposed in 1996 by Ari et al. [18]: Fig. 1.7-a and 1.7-b show 6-6 GS platforms with six RUS legs and six PSS legs respectively. The first platform features high dynamic characteristics since the actuators are fixed to the base, whereas the second one was designed to work accurately and to perform high speed tasks.

In 1997 Honegger at al. [19] presented the dynamic equation, nonlinear control and dynamic parameters identification of the Hexaglide (Fig. 1.8): a 6-6 GS platform with six PUS legs studied for a high-speed milling machine.

In 1998 Ji et al., given the low mobility of parallel manipulator with respect to the serial ones, proposed a reconfigurable platform [20] (Fig. 1.9), that is composed by modular links and joints and can be adapted to perform different tasks. The new six UPUR legs 6-6 GS platform can be reconfigured by means of some holes placed on the mobile platform and the fixed base, which are used as connections for the legs.

Commercial products

Several commercial GS platforms are available under the name of hexapods. Some of those are built for specific applications, like flight simulators or machine-tools whose size and performance poorly match the requirement of the in vitro loading system. Others are

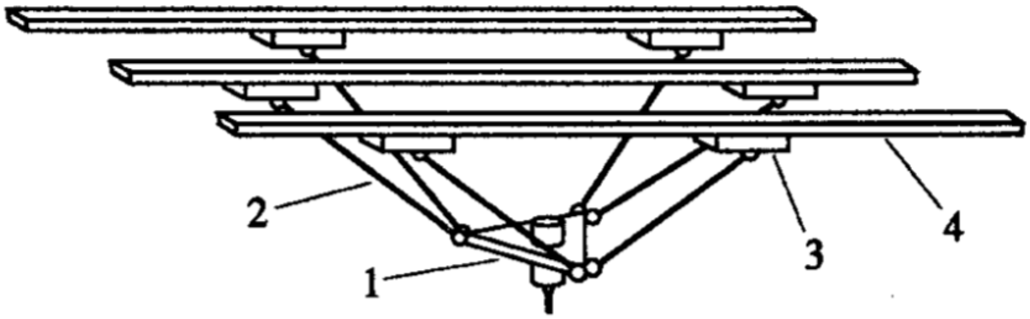

Figure 1.8. Schematic representation of the Hexaglide [19].

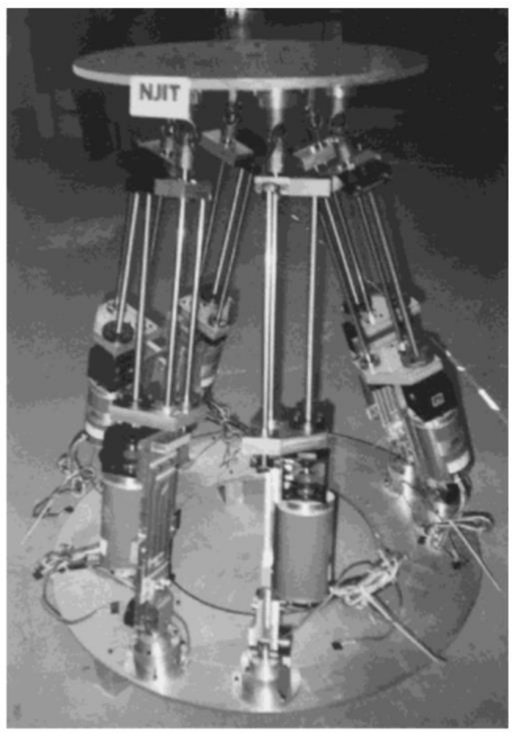

Figure 1.9. Reconfigurable manipulator proposed by Ji et al. [20].

built to be adaptable to a wider range of applications; six-DOF parallel manipulators are offered by two main companies: Fanuc and Symétrie.

Fanuc is one of the most famous company working on automation and proposes many manipulators, especially serial ones, and CNC systems. Symétrie has a special focus in the construction of Hexapods, that proposes in different sizes and characteristics so that it can be adaptable in a very wide range of situations: automation, astronomy, energy sector and oil behavior simulations.

The products that would have been best suited to the case under study (i.e. test rig machines for human joint simulation) are (Fig. 1.10):

1. 6-3 GS platform-based manipulator Fanuc F-200iB (Fig. 1.10-a) [21];
2. 6-3 GS platform-based manipulator Fanuc F-100 (Fig. 1.10-b) [22];
3. 6-6 GS platform-based manipulator Symétrie NOTUS P (Fig. 1.10-c) [23].

Further information about the performances of these manipulators are shown on the related brochures [21-23].

The Fanuc manipulators are used on a variety of manufacturing and automotive system processes. They are designed for applications that need extreme rigidity and high repeatability. The maximum reachable payload by the F-200iB and the F-100 is 1000 N and 2500 N respectively. The Symétrie NOTUS P is mainly used to test devices under specific motion conditions (e.g. swell motion and vibrations) and reach a payload of 2000N.

Though these commercial products are very efficient, they poorly fit the loading system requirements of a test rig for human joints. Indeed, they are exclusively engineered to operate under motion control and they cannot be adapted to work under force control unless extremely complex and unprofitable solutions are considered.

a) b) c)

Figure 1.10. a) Fanuc F-200iB courtesy of Fanuc; b) Fanuc F-100 courtesy of Fanuc; c) NOTUS courtesy of Symétrie.

Moreover, the maximum admissible payload is too low for the conditions that need to be studied during the in vitro test: preliminary studies show that the quadriceps muscle, during daily life motion tasks, applies on the tibia a force of 3000 N and this force is transferred directly to the manipulator.

The new manipulator

In this thesis, a new GS platform-based manipulator (Fig. 1.11) is proposed. It is composed of a mobile platform and a fixed base that are connected by three 2U2P2RU kinematic chains. The new manipulator can be seen as an evolution of the Fanuc F-200iB manipulator. Indeed, it features some modifications that can be very useful when a high stiffness is required:

1. the new platform is a six-DOF overconstrained manipulator: the overall number of kinematic pairs is lower than that of the 6-6 GS platform and the Fanuc manipulator.

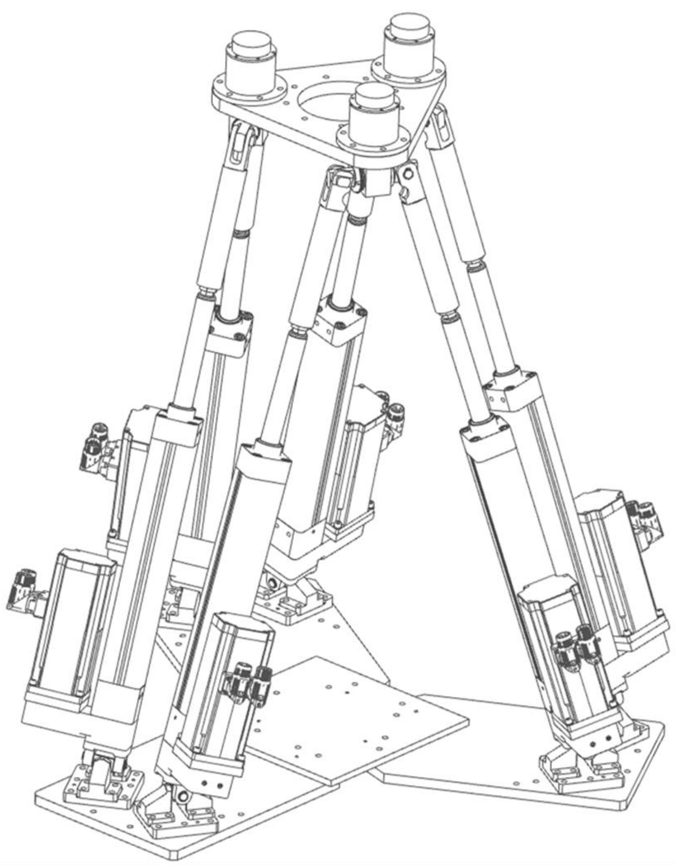

Figure 1.11. Tridimensional representation of the manipulator.

2. spherical joints are avoided; generally speaking, physical S joints have a reduced mobility and, thus, limit the workspace of the manipulator.
3. thrust bearings (revolute joints in which the load acts along the rotation axis) are also avoided. In most cases, when the S joints cannot be used (because of their low mobility), they are substituted by three R joints with concurrent axes, generally a U joint plus a thrust bearing. In this case, the manufacturing of the manipulator can be very demanding unless an under-performing solution is considered.
4. Particular connections patented by Fanuc, called “locator pivot” joints [24], are used between the actuators and the platform. This makes it possible to mount some high precision but bulky load cells (Fig. 1.12) without compromising the dexterous workspace.

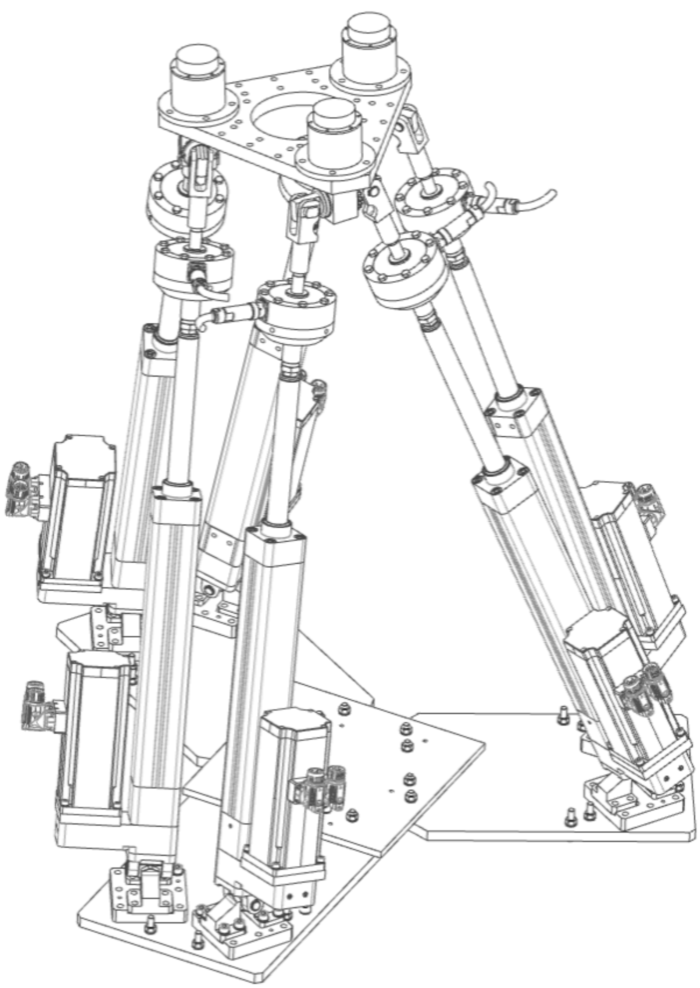

Figure 1.12. Tridimensional representation of the manipulator with load cells.

In the following chapters, the new manipulator is described and the following analyses are performed:

1. position, velocity and static analyses. In particular, the solution of the position analysis problem is shown, and the Jacobian matrix is determined;

2. numerical workspace analysis (methods and results). In particular, the volume in which the platform (end-effector) with some fixed orientations can move is found, considering the collision and the limits of the actuation;

3. numerical singularity analysis. For some fixed orientations of the platform (the same used for the workspace analysis), the singularity surfaces are numerically determined;

4. singularity characterization. A geometrical explanation of the singular configurations found is given using the Grassmann-Cayley Algebra;

5. manufacturing solution analysis. A workspace analysis is conducted that takes into account the mobility of the passive joints obtained by the chosen design.

CHAPTER 2 – DIMENSIONING

Test rig functioning

In this chapter, the procedure used to determine the proper geometry of the manipulator is described. For the sake of clarity, a detailed explanation of the test rig functioning is given.

The new machine features three main parts (Fig. 2.1): a frame (4), a loading system (2, 3, and 11), and a portal (9). The platform (3) is connected to the tibia (5) by a six-DOF fixation system (10). The femur (7) has a similar connection (6) with the portal. Both fixation systems are unactuated and make it possible to precisely control the femur–portal and tibia-platform relative poses for a precise alignment of the specimen.

The portal is actuated and is connected to the frame by means of a revolute joint O. The rotation of the portal is responsible of the knee flexion. Indeed, the alignment of the revolute joint axis and the knee flexion axis is made, approximately, with the femur

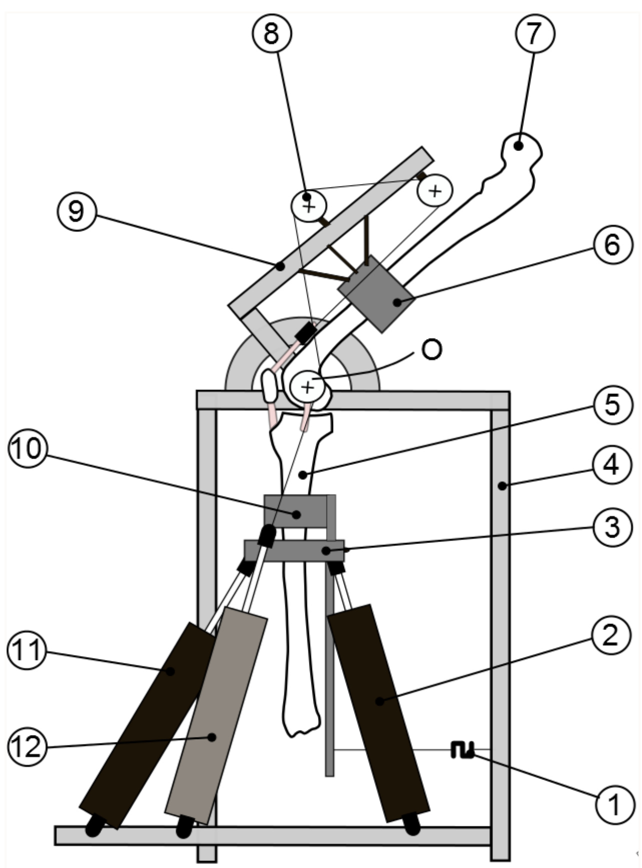

Figure 2.1. Test rig: two-dimensional representation.

fixation system (6): 150 deg of flexion can be obtained by rotating the portal. While the femur rotates, the tibia must remain vertical, namely, its rotation about the knee flexion axis has to be null.

For all the other five DOFs, the tibia, at a given flexion angle, is free to move, according to the constraints given by the anatomical structures and to the loads imposed by the loading system. As a result, for a given flexion angle, the prescribed loads are applied, and the tibia can move to find the balance position.

The loading system is a force-controlled manipulator so that it can apply the wanted loads in real time with the joint flexion angle to reproduce the task loading conditions. The tibia axis is kept vertical by the application of specific additional loads that simulate the muscle forces. Two opposed load cells (1) connected to the frame by two wires allow measuring the force generated by the moment flexion/extension component, due to the loads applied by the loading system. The muscle forces make it possible to maintain load cell force (and consequently, the unbalanced moment flexion/extension component) equal to zero. In particular, if the tibia tends to flex due to the external loads, an extensor torque is applied by a system composed of an actuator (12) and a set of pulleys (8) that simulates the quadriceps muscle force. On the other hand, if the tibia tends to extend, flexor muscle forces are exerted by the loading system itself and added to the external loads. The muscle force contribution is thus computed and applied in real time rather than being known a priori [3].

A research in the literature was performed to figure out what are the loads to which the human joints are subjected to, and their relative movements, when performing daily life and sport activities. The common motion tasks considered in the literature are:

1. squat [25];
2. sit-to-stand [26];
3. walking [27];
4. running and cutting maneuvers [28,29].

The relative papers [25-29] report data about the ground reaction forces and about the relative pose between the bones of the joints as function of the flexion angle that are used in the simulations for the dimensioning of the manipulator. Also, the results of the tests conducted on the knee with the previous GRAB test rig are considered, especially in the determination of the quadriceps muscle force that is applied on the tibia (3000N) [3].

Dimensioning of the manipulator

Given the general context, more in detail, the following conditions need to be granted for the loading system:

1. application of several loading conditions: since the test rig is used to simulate several motion tasks, the loading system must allow the application of the related loading conditions, some of which are demanding and required the actuators to exert very high forces;
2. a minimum functioning workspace: considering the mobility of human joints under both healthy and pathological situations, the loading system must allow ± 30° of rotation about ab/adduction and intra/extra rotation axis, ± 10° of rotation about the flexion/extension axis (even though it is supposed to be zero, since this rotation about that axis is controlled by the portal), ± 10 mm of medial–lateral displacement, and ± 40 mm of anterior–posterior and distraction displacements, in order not to constrain the tibia during standard loaded tasks. In the following chapters this workspace is represented as a rectangle parallelepiped whose position on space depends on the position and shape of the workspace of the manipulator;
3. a free-from-singularities workspace: singular conditions are those configurations in which the manipulator gains one or more degrees of freedom, so it cannot be controlled and, thus, the required loading conditions cannot be applied to the tibia. A manipulator that has singular configurations in the workspace is not compatible with the loading system.

Briefly, the new manipulator can be seen as a fixed plate and a mobile plate connected by three kinematic chains. The connections of the kinematic chains with the mobile plate are identified by the points C_i (i=1,2,3), whereas the connections with the fixed plate are identified by the points $A_{i,j}$ (i=1,2,3, j=1,2). Varying the geometry of the manipulator and thus the relative position between the connection points, the required specifications for the loading system can be reached. The following geometric parameters are chosen in order to find the optimized geometry (Fig. 2.2):

1. d_b diameter of the circle along which the points $A_{i,j}$ are placed;
2. d_p diameter of the circle along which the points C_i are placed;
3. φ_b offset (positive or negative) of the points $A_{i,j}$, two by two, with respect to three axes at 120°;
4. l distance between the two R joint parallel axes belonging to a single pivot joint (briefly, with reference to Fig. 2.3, the connection is constituted by four revolute joints): these axes connect the actuators of the same kinematic chain to the pivot joint (a more detailed explanation of the pivot joint is given in the next chapter).

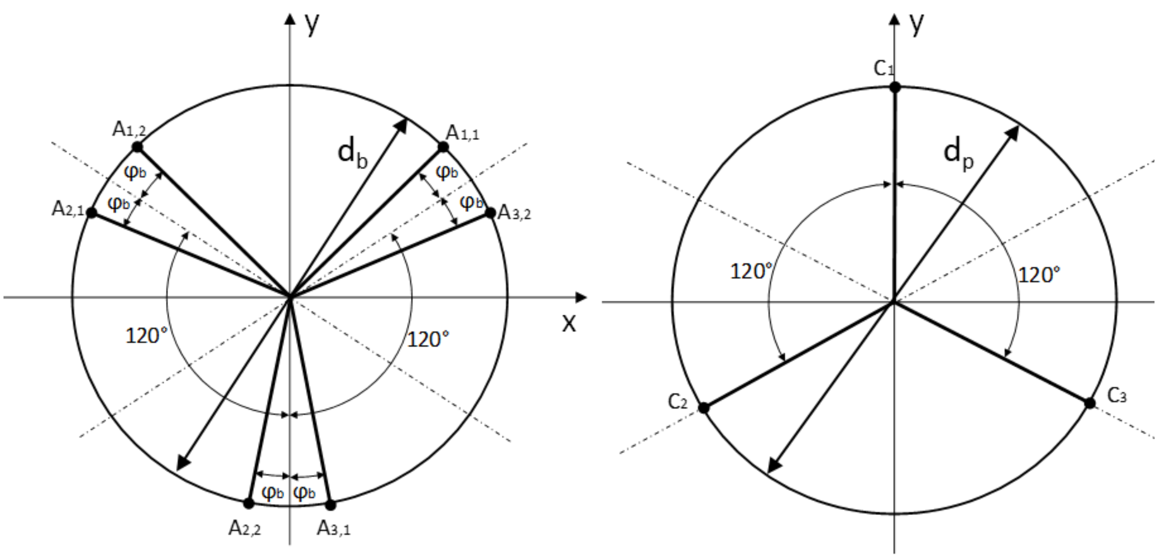

Figure 2.2. Position of the connection points $A_{i,j}$ and points C_i.

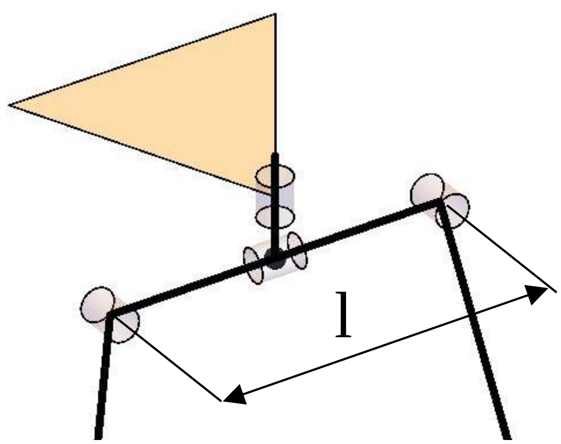

Figure 2.3. pivot joint schematic representation, the triangular element represents the mobile platform defined by the point C_i.

Other characteristics of the manipulator are given:

1. maximum and minimum elongation of the actuators and the maximum force they can exert;
2. dimension of the load cells;

The actuators mounted on the manipulator are linear ballscrew Parker electrocylinders, model ETH05M05C1K1CCSN0300B (Fig. 2.4). They have been chosen because of their sensibility and resistance to lateral forces (principal characteristics are reported in detail in attachment A.1).

Tension/compression load cells HBM U10M have been chosen. These load cells guarantee high accuracy and a very wide range of measurements (± 5000 N in dynamic condition), but, as a drawback, they are bulky (they can be represented as cylinders with a diameter of 104.8 mm and height of 60.3 mm), thus they can limit the workspace of the manipulator (main characteristics are reported in details in attachment A.2).

The procedure adopted to determine the appropriate geometry for the mechanism uses the results obtained from:

1. static analysis;
2. workspace analysis;
3. singularity analysis;
4. mechanical design.

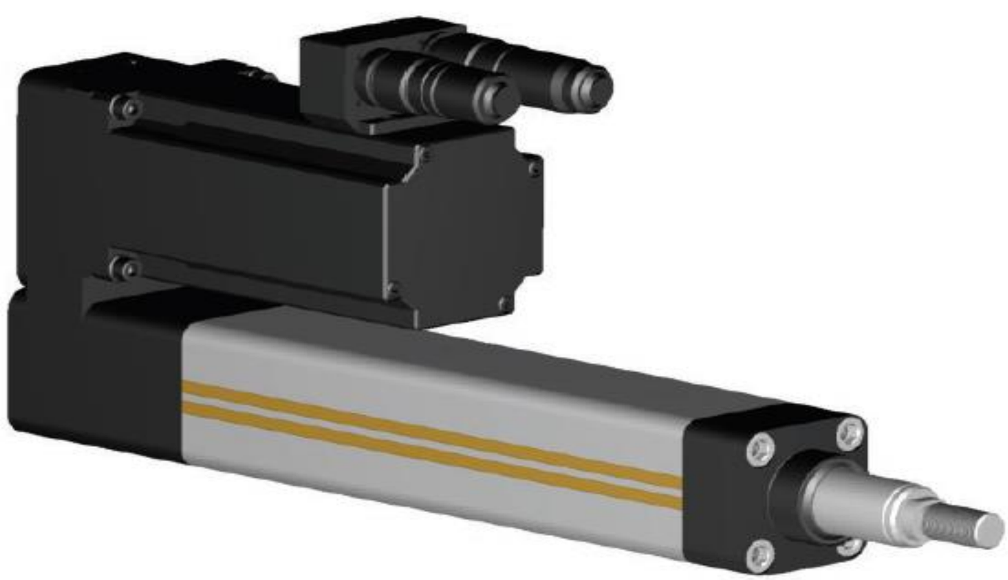

Figure 2.4. Parker electrocylinder actuator.

Static analysis aims at finding the forces that the actuators must exert in order to replicate the loading conditions on the tibia for a given motion task. As previously mentioned, since several loading conditions must be examined, the highest ones are considered for computations. For a starting set of values of the geometric parameters, static analysis is conducted and the maximum value of the modulus of the forces of the actuators is used to compare the results. The geometry that shows the minimum value of the maximum force is chosen. The maximum value of the forces can be higher than the maximum value allowable by the load cell (namely, 5000 N): the aim of the static analysis is to determine a geometry for the manipulator that can grant the wider possible range of loading conditions applicable during in vitro tests, given that the standard tasks (namely, those that can be studied with the existing in vitro test rigs) can be easily simulated.

Thereafter, for the chosen geometry a verification phase is performed: the workspace and singularity analyses are conducted, to verify whether the workspace of the manipulator obtained is compatible with the minimum operating space needed for the in vitro test (in this computation only the maximum and minimum elongation of the actuators and possible collisions between the load cells are considered as constraints) and whether it is free from singularities. Actually, static and workspace analyses must be performed simultaneously since some data from the workspace analysis are used to evaluate the static behavior of the manipulator.

Moreover, the mechanical design is developed so as to understand if the geometry chosen is compatible with a real construction of the manipulator: the joints need to be properly designed to have the required mobility. A new workspace analysis that include the limitations given by the passive joint mobility is conducted.

Whenever each analysis of the verification phase gives a negative result and since some geometries are excluded, the procedure starts again from the beginning using another set of starting values of the geometric parameters whose range of variation is smaller than the previous one.

The manipulator geometries considered in the very first step are those that can be obtained from all the combinations of the parameters listed in the following (dimensions are express in m):

1. d_b = [0.6 0.65 0.7 0.75 0.8 0.85 0.9 0.95 1];

2. d_p = [0.1 0.15 0.2 0.25 0.3 0.35 0.4];
3. φ_b = [5° 6° 7° 8° 9° 10°];
4. l = [0.005 0.01 0.015 0.02 0.025 0.03].

In general, given the dimension of the mobile platform, bigger is the fixed base better is the static behavior of the manipulator, but smaller is its dexterous workspace: the procedure aims at finding the best compromise between the two characteristics.

It is obvious that this procedure does not lead to a unique solution. Several geometries, diversified mainly for the mechanical constructive solutions adopted, were obtained. A fundamental role was played by the machine tools capability and availability at disposal that helped to reach the final result. Therefore, it is not possible to exactly report the path that led to the solution adopted, and, thus, only the final geometry is shown.

The following geometric parameters for the manipulator are obtained at the end:

1. d_b = 0.832 m;
2. d_p = 0.28 m;
3. φ_b = 9.7°;
4. l = 0.01 m.

In the following chapters, the analyses used in the dimensioning procedure are described and the results are shown only for the manipulator with the final geometry. Where not specified unit for lengths are in meters, while for rotations in degrees.

CHAPTER 3 - THE NEW GOUGH-STEWART PLATFORM

Introduction

This chapter deals with the description of the new manipulator. At the beginning, the geometrical description of the manipulator and the mobility analysis are given. It is proven that the mechanism has six DOFs contrary to the mobility formula. Then, position and velocity analysis are shown, and the Jacobian matrix is determined.

Description of the mechanism

The mechanism is composed of a mobile platform (1) (Fig. 3.1) and a fixed base (2) connected by three 2U2P2RU close-loop kinematic chains (Fig. 3.2). The mobile platform has three connection points C_i, i=1,2,3, that define a plane σ, whereas the fixed base has six connection points $A_{i,j}$, i=1,2,3, j=1,2, that lie on a plane π. Each kinematic chain is defined by the points $A_{i,1}$, $A_{i,2}$, $B_{i,2}$, $B_{i,1}$. The middle point of the upper link $B_{i,2}B_{i,1}$ of the i-th kinematic chains is connected to the mobile platform by a U joint

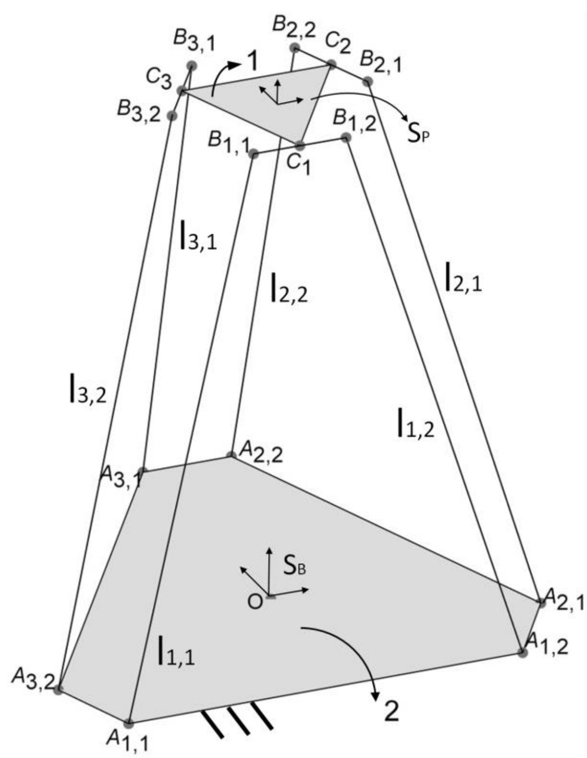

Figure 3.1. Schematic representation of the manipulator.

centered at point C_i. The ends (points $B_{i,2}$ and $B_{i,1}$) of upper link are connected to the actuators $A_{i,1}B_{i,1}$ and $A_{i,2}B_{i,2}$ by means of R joints. The actuators are P joints and are connected to the other ends (points $A_{i,2}$ and $A_{i,1}$) to the fixed base by means of U joints (Fig. 3.2). A particular geometrical condition is needed: R joint axes and the mobile U joint axes are parallel, while the fixed U joint axes are collinear. Specifically, the fixed axes coincide with ρ_i that is the axis passing through the points $A_{i,2}$ and $A_{i,1}$ (Fig. 3.2). Due to the parallelism condition of the axes described above, the i-th kinematic chains lies on a plane γ_i, that is the plane passing through the points C_i, $A_{i,1}$, $A_{i,2}$. This condition occurs for any configuration of the mobile platform.

Mobility analysis

The degrees of freedom that the mobile platform has with respect to the fixed base can be found according to the mobility formula for a mechanism in space:

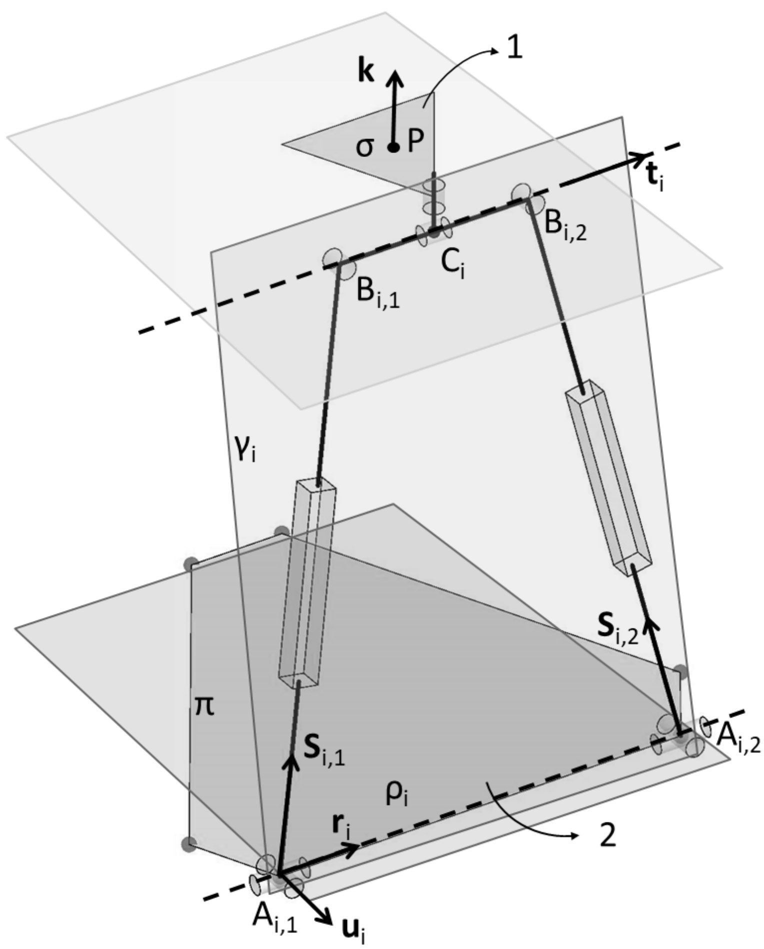

Figure 3.2. Schematic representation of one connection leg.

$$n_s = 6(n_l - 1) - \sum_{i=1}^{5}(6-i)n_{k,i} = 6 \cdot 16 - 12 \cdot 5 - 9 \cdot 4 = 0 \qquad (1)$$

Where the following quantities are used:

- n_s is the number of DOFs of the mechanism;
- n_l is the number of links;
- $n_{k,i}$ is the number of kinematic pairs that allow i DOFs in space.

Even though from the mobility formula seems that the manipulator is a structure (it can't move since it has zero DOFs), it is easy to prove that the mechanism has actually six DOFs. The proof consists on showing that each connection between the mobile platform and the fixed base provides six DOFs and, consequently, the mobile platform has six DOFs with respect to the fixed base.

If the linear actuators are locked, each kinematic chain is equivalent to a planar four-bar linkage on γ_i defined by the segment links $A_{i,1}B_{i,1}$, $B_{i,1}B_{i,2}$, $B_{i,2}A_{i,2}$ and $A_{i,2}A_{i,1}$, and by the two R joints at points $B_{i,1}$ and $B_{i,2}$, and by the mobile axes of the U joints at points $A_{i,1}$ and $A_{i,2}$.

Since the length of vectors $\mathbf{A}_{i,1}\mathbf{B}_{i,1}$ and $\mathbf{A}_{i,2}\mathbf{B}_{i,2}$ can be changed by means of the P joints, the number of DOFs of each kinematic chain (considered on the plane γ_i) is three. Moreover, the collinear axis of the U joints allows the three DOFs planar linkage to rotate about the ρ_i axis at points $A_{i,1}$ and $A_{i,2}$. Finally, other two DOFs are provided to the linkage via the U joints at points C_i. Thus, each kinematic chain grants six DOFs to the platform and, thus, the mechanism has six DOFs that are controlled by the six linear actuators, two for each kinematic chain.

Position Analysis

The position analysis problem is to determine the length of the actuators given the configuration of the platform (inverse position analysis), and to determine the configuration of the mobile platform given the length of the actuators (direct position analysis). If the first problem is very easy to solve, the second one is more difficult. In this paragraph the solution of the position analysis problem is shown.

The configuration of the platform with respect to the base can be expressed by the position vector $\mathbf{p}$ of a point P of the platform and by the 3-by-3 rotation matrix ${}^{b}\mathbf{R}_{p}$, that describes the transformation of vector components from S_p to S_b (Fig.3.2). S_b to S_p are two Cartesian coordinate systems attached to the base and the platform respectively.
The transformation matrix ${}^{b}\mathbf{R}_{p}$ is defined as follows:

$$ {}^{b}\mathbf{R}_{p} = \mathbf{R}_{x}(\eta)\mathbf{R}_{z}(\varphi)\mathbf{R}_{y}(\psi) \tag{2} $$

where $\mathbf{R}_{\delta}(\beta)$ is the elementary rotation about the δ axis of the β quantity.
For the sake of clarity, hereinafter this general annotation applies to the vectors: **AB** express the vector that goes from point A to point B. Moreover, the following quantities are identified (Fig.3.1 and Fig. 3.2):

- $l_{i,j}$ and $\mathbf{s}_{i,j}$ are the length and the unit vectors of the j-th (j=1,2) link of the i-th (i=1,2,3) kinematic chain (i.e., $l_{i,j}=\|\mathbf{A}_{i,j}\mathbf{B}_{i,j}\|$, $\mathbf{s}_{i,j}=\mathbf{A}_{i,j}\mathbf{B}_{i,j}/l_{i,j}$);
- l and $\mathbf{t}_i$ are the length and the unit vectors of the i-th upper link (i.e., $l=\|\mathbf{B}_{i,1}\mathbf{B}_{i,2}\|$, $\mathbf{t}_i=\mathbf{B}_{i,1}\mathbf{B}_{i,2}/l$);
- $\mathbf{r}_i$ is the unit vector of the i-th lower link (i.e., $\mathbf{r}_i=\mathbf{A}_{i,1}\mathbf{A}_{i,2}$);
- $\mathbf{k}$ is the unit vector normal to the plane σ;
- $\mathbf{d}_i=\mathbf{A}_{i,1}\mathbf{C}_i$;
- $\mathbf{u}_i=(\mathbf{r}_i \times \mathbf{d}_i)/\|\mathbf{r}_i \times \mathbf{d}_i\|$ is the unit vector normal to the plane γ_i.

For each actuator the following closure equation can be written:

$$ \boldsymbol{p} + {}^{b}\mathbf{R}_{p}\, {}^{p}\mathbf{c}_{i} = \mathbf{OA}_{i,j} + \mathbf{A}_{i,j}\mathbf{B}_{i,j} + \mathbf{B}_{i,j}\mathbf{C}_{i} = \mathbf{OA}_{i,j} + \mathbf{l}_{i,j}\mathbf{s}_{i,j} \pm \frac{\mathbf{l}}{\mathbf{2}}\mathbf{t}_{i} \tag{3} $$

Where ${}^{p}\mathbf{c}_i$ expresses the vector $\mathbf{PC}_i$ represented in S_p (hereafter, for the vector represented in S_b, the superscript b is omitted) and where the symbol $\pm$ is - when j=1, + when j=2. In the following analysis the symbol $\pm$ is replaced by + for the sake of simplicity. Rewriting and squaring (3), the following algebraic equation can be obtained:

$$ (l_{i,j}s_{i,j})^{T}(l_{i,j}s_{i,j}) = l_{i,j}{}^{2} = $$

$$ (-\boldsymbol{p} - {}^{b}\boldsymbol{R}_{p}\, {}^{p}\boldsymbol{c}_{i} + \boldsymbol{OA}_{i,j} + \frac{\boldsymbol{l}}{\mathbf{2}}\boldsymbol{t}_{i})^{\boldsymbol{T}}(-\boldsymbol{p} - {}^{b}\boldsymbol{R}_{p}\, {}^{p}\boldsymbol{c}_{i} + \boldsymbol{OA}_{i,j} + \frac{\boldsymbol{l}}{\mathbf{2}}\boldsymbol{t}_{i}) \tag{4} $$

For the constraint described above, $\mathbf{B}_{i,1}\mathbf{B}_{i,2}$ lies both on plane γ_i and on plane σ, the direction of the unit vector $\mathbf{t}_i$ is given by the vector product of the vectors normal to those planes. Since $\mathbf{r}_i$ x $\mathbf{d}_i$ is a vector normal to the plane γ_i, $\mathbf{t}_i$ can be written as:

$$\boldsymbol{t_i} = \frac{\boldsymbol{k}\times(\boldsymbol{r}_i\times\boldsymbol{d}_i)}{\|\boldsymbol{k}\times(\boldsymbol{r}_i\times\boldsymbol{d}_i)\|} = \frac{{}^b\boldsymbol{R}_p\,{}^p\boldsymbol{k}\times(\boldsymbol{r}_i\times(\boldsymbol{p}+{}^b\boldsymbol{R}_p\,{}^p\boldsymbol{c}_i))}{\left\|{}^b\boldsymbol{R}_p\,{}^p\boldsymbol{k}\times(\boldsymbol{r}_i\times(\boldsymbol{p}+{}^b\boldsymbol{R}_p\,{}^p\boldsymbol{c}_i))\right\|} \tag{5}$$

Inserting relation (5) in (4), it is possible to obtain an expression in which only the components of the position vector $\mathbf{p}$ (p_x, p_y and p_z) and the three parameters defining the rotation matrix ${}^b\mathbf{R}_p$ (η, φ and ψ) appear. The other vectors which appear in the equation are given once the geometry of the manipulator is chosen. Therefore, considering the corresponding closure equations (4) associated with the length $l_{i,j}$ six times (i=1,2,3, j=1,2,), a system of six equations in six unknowns (p_x, p_y, p_z, η, φ and ψ) can be assembled.

Velocity and static analysis

Differentiating with respect to time and projecting each term of equation (3) on $\mathbf{s}_{i,j}$, the following relation is obtained:

$$\boldsymbol{v}_{c_i}\cdot\boldsymbol{s}_{i,j} = \dot{l}_{i,j} + \frac{\boldsymbol{l}}{\boldsymbol{2}}\frac{\boldsymbol{dt}_i}{\boldsymbol{dt}}\cdot\boldsymbol{s}_{i,j} \tag{6}$$

where $\boldsymbol{\omega}$ is the platform angular velocity, and

$$\frac{d\boldsymbol{t}_i}{dt}\cdot\boldsymbol{s}_{i,j} = \frac{d}{dt}\left(\frac{\boldsymbol{k}\times(\boldsymbol{r}_i\times\boldsymbol{d}_i)}{\|\boldsymbol{k}\times(\boldsymbol{r}_i\times\boldsymbol{d}_i)\|}\right)\cdot\boldsymbol{s}_{i,j} = \frac{d}{dt}\left(\frac{\boldsymbol{w}_i}{\|\boldsymbol{w}_i\|}\right)\cdot\boldsymbol{s}_{i,j} \tag{7}$$

where $\mathbf{w}_i = [\mathbf{k}\times(\mathbf{r}_i\times\mathbf{d}_i)]$ to simplify the following derivation. Therefore:

$$\frac{d}{dt}\left(\frac{\boldsymbol{w}_i}{\|\boldsymbol{w}_i\|}\right)\cdot\boldsymbol{s}_{i,j} = \left(\frac{\frac{d\boldsymbol{w}_i}{dt}\|\boldsymbol{w}_i\| - \boldsymbol{w}_i\frac{d(\|\boldsymbol{w}_i\|)}{dt}}{\|\boldsymbol{w}_i\|}\right)\cdot\boldsymbol{s}_{i,j} \tag{8}$$

In particular:

$$\frac{d}{dt}(\|\boldsymbol{w}_i\|) = \frac{d}{dt}\left(\sqrt{\boldsymbol{w}_i \cdot \boldsymbol{w}_i}\right) = \frac{1}{2}\frac{1}{\sqrt{\boldsymbol{w}_i \cdot \boldsymbol{w}_i}}\left(2\boldsymbol{w}_i \cdot \frac{d\boldsymbol{w}_i}{dt}\right) = \frac{1}{\|\boldsymbol{w}_i\|}\left(\boldsymbol{w}_i \cdot \frac{d\boldsymbol{w}_i}{dt}\right) \tag{9}$$

Thus, substituting (9) in (7):

$$\frac{\mathrm{d}}{\mathrm{dt}}\left(\frac{\mathbf{w}_\mathrm{i}}{\|\mathbf{w}_\mathrm{i}\|}\right) \cdot \mathbf{s}_{\mathrm{i,j}} = \left(\frac{\frac{\mathrm{d}\mathbf{w}_\mathrm{i}}{\mathrm{dt}}\|\mathbf{w}_\mathrm{i}\| - \mathbf{w}_\mathrm{i}\left(\frac{1}{\|\mathbf{w}_\mathrm{i}\|}\left(\mathbf{w}_\mathrm{i} \cdot \frac{\mathrm{d}\mathbf{w}_\mathrm{i}}{\mathrm{dt}}\right)\right)}{\|\mathbf{w}_\mathrm{i}\|}\right) \cdot \mathbf{s}_{\mathrm{i,j}} = \frac{\frac{\mathrm{d}\mathbf{w}_\mathrm{i}}{\mathrm{dt}}}{\|\mathbf{w}_\mathrm{i}\|}\left(\mathbf{s}_{\mathrm{i,j}} - \frac{\mathbf{w}_\mathrm{i}(\mathbf{w}_\mathrm{i} \cdot \mathbf{s}_{\mathrm{i,j}})}{\|\mathbf{w}_\mathrm{i}\|^2}\right) =$$

$$\frac{\frac{\mathrm{d}\mathbf{w}_\mathrm{i}}{\mathrm{dt}}}{\|\mathbf{w}_\mathrm{i}\|}\left(\mathbf{s}_{\mathrm{i,j}} - \mathbf{t}_\mathrm{i}(\mathbf{t}_\mathrm{i} \cdot \mathbf{s}_{\mathrm{i,j}})\right) = \frac{\frac{\mathrm{d}\mathbf{w}_\mathrm{i}}{\mathrm{dt}}}{\|\mathbf{w}_\mathrm{i}\|} \cdot \mathbf{h}_{\mathrm{i,j}} \tag{10}$$

Moreover,

$$\frac{\mathrm{d}\mathbf{w}_\mathrm{i}}{\mathrm{dt}} = \frac{\mathrm{d}\mathbf{k}}{\mathrm{dt}} \times (\mathbf{r}_\mathrm{i} \times \mathbf{d}_\mathrm{i}) + \mathbf{k} \times \frac{\mathrm{d}}{\mathrm{dt}}(\mathbf{r}_\mathrm{i} \times \mathbf{d}_\mathrm{i})$$
$$= (\boldsymbol{\omega} \times \mathbf{k}) \times (\mathbf{r}_\mathrm{i} \times \mathbf{d}_\mathrm{i}) + \mathbf{k} \times \left(\mathbf{r}_\mathrm{i} \times \mathbf{v}_{\mathrm{c}_\mathrm{i}}\right) \tag{11}$$

Substituting (11) in (10), and for the properties of the triple product:

$$\frac{1}{\|\mathbf{w}_\mathrm{i}\|}\frac{\mathrm{d}\mathbf{w}_\mathrm{i}}{\mathrm{dt}} \cdot \mathbf{h}_{\mathrm{i,j}} = \frac{1}{\|\mathbf{w}_\mathrm{i}\|}\left((\boldsymbol{\omega} \times \mathbf{k}) \times (\mathbf{r}_\mathrm{i} \times \mathbf{d}_\mathrm{i}) + \mathbf{k} \times \left(\mathbf{r}_\mathrm{i} \times \mathbf{v}_{\mathrm{c}_\mathrm{i}}\right)\right) \cdot \mathbf{h}_{\mathrm{i,j}} =$$

$$\frac{1}{\|\mathbf{w}_\mathrm{i}\|}(\boldsymbol{\omega} \times \mathbf{k})\left((\mathbf{r}_\mathrm{i} \times \mathbf{d}_\mathrm{i}) \times \mathbf{h}_{\mathrm{i,j}}\right) + \frac{1}{\|\mathbf{w}_\mathrm{i}\|}\left(\mathbf{r}_\mathrm{i} \times \mathbf{v}_{\mathrm{c}_\mathrm{i}}\right)\left(\mathbf{k} \times \mathbf{h}_{\mathrm{i,j}}\right) =$$

$$\frac{1}{\|\mathbf{w}_\mathrm{i}\|}\boldsymbol{\omega} \cdot \left(\mathbf{k} \times \left((\mathbf{r}_\mathrm{i} \times \mathbf{d}_\mathrm{i}) \times \mathbf{h}_{\mathrm{i,j}}\right)\right) + \frac{1}{\|\mathbf{w}_\mathrm{i}\|}\mathbf{v}_{\mathrm{c}_\mathrm{i}} \cdot \left(\left(\mathbf{h}_{\mathrm{i,j}} \times \mathbf{k}\right) \times \mathbf{r}_\mathrm{i}\right) \tag{12}$$

Therefore, (6) becomes

$$\mathbf{v}_{\mathrm{c}_\mathrm{i}} \cdot \mathbf{s}_{\mathrm{i,j}}$$
$$= \dot{\mathrm{l}}_{\mathrm{i,j}} + \frac{\mathrm{l}}{2}\frac{1}{\|\mathbf{w}_\mathrm{i}\|}\boldsymbol{\omega} \cdot \left(\mathbf{k} \times \left((\mathbf{r}_\mathrm{i} \times \mathbf{d}_\mathrm{i}) \times \mathbf{h}_{\mathrm{i,j}}\right)\right) + \frac{\mathrm{l}}{2}\frac{1}{\|\mathbf{w}_\mathrm{i}\|}\mathbf{v}_{\mathrm{c}_\mathrm{i}} \cdot \left(\left(\mathbf{h}_{\mathrm{i,j}} \times \mathbf{k}\right) \times \mathbf{r}_\mathrm{i}\right) \tag{13}$$

$$-\boldsymbol{\omega}\cdot\left(\mathbf{k}\times\left((\mathbf{r}_\mathrm{i}\times\mathbf{d}_\mathrm{i})\times\mathbf{h}_\mathrm{i,j}\right)\right)\frac{\mathrm{l}}{2}\frac{1}{\|\mathbf{w}_\mathrm{i}\|}-\mathbf{v}_{\mathrm{c}_\mathrm{i}}\cdot\left(\left((\mathbf{h}_\mathrm{i,j}\times\mathbf{k})\times\mathbf{r}_\mathrm{i}\right)\frac{\mathrm{l}}{2}\frac{1}{\|\mathbf{w}_\mathrm{i}\|}-\mathbf{s}_\mathrm{i,j}\right)$$

$$=\boldsymbol{\omega}\cdot\mathbf{f}_\mathrm{i,j}+\mathbf{v}_{\mathrm{c}_\mathrm{i}}\cdot\mathbf{q}_\mathrm{i,j}=\dot{\mathrm{l}}_\mathrm{i,j} \tag{14}$$

where

$$\mathbf{f}_\mathrm{i,j}=\left(\mathbf{k}\times\left((\mathbf{r}_\mathrm{i}\times\mathbf{d}_\mathrm{i})\times\mathbf{h}_\mathrm{i,j}\right)\right)\frac{\mathrm{l}}{2}\frac{1}{\|\mathbf{w}_\mathrm{i}\|}$$

$$\mathbf{q}_\mathrm{i,j}=-\left(\left((\mathbf{h}_\mathrm{i,j}\times\mathbf{k})\times\mathbf{r}_\mathrm{i}\right)\frac{\mathrm{l}}{2}\frac{1}{\|\mathbf{w}_\mathrm{i}\|}-\mathbf{s}_\mathrm{i,j}\right) \tag{15}$$

to simplify the notation. Considering that:

$$\mathbf{v}_{\mathrm{c}_\mathrm{i}}=\dot{\mathbf{p}}+\boldsymbol{\omega}\times\mathbf{PC}_\mathrm{i} \tag{16}$$

equation (14) becomes:

$$\boldsymbol{\omega}\cdot\mathbf{f}_\mathrm{i,j}+(\dot{\mathbf{p}}+\boldsymbol{\omega}\times\mathbf{PC}_\mathrm{i})\cdot\mathbf{q}_\mathrm{i,j}=\boldsymbol{\omega}\cdot\left(\mathbf{f}_\mathrm{i,j}+\mathbf{PC}_\mathrm{i}\times\mathbf{q}_\mathrm{i,j}\right)+\dot{\mathbf{p}}\cdot\mathbf{q}_\mathrm{i,j}=\dot{\mathrm{l}}_\mathrm{i,j} \tag{17}$$

This relation can be written for all the six actuators giving the following matrix system:

$$\begin{pmatrix}\mathbf{q}_{1,1} & \mathbf{f}_{1,1}+\mathbf{PC}_1\times\mathbf{q}_{1,1}\\ \vdots & \vdots\\ \mathbf{q}_{3,2} & \mathbf{f}_{3,2}+\mathbf{PC}_3\times\mathbf{q}_{3,2}\end{pmatrix}\begin{pmatrix}\dot{\mathbf{p}}\\ \boldsymbol{\omega}\end{pmatrix}=\begin{pmatrix}\dot{\mathrm{l}}_{1,1,}\\ \vdots\\ \dot{\mathrm{l}}_{3,2}\end{pmatrix} \tag{18}$$

Relation (18) expresses the relation between the joint velocities $\dot{l}_{i,j}$ and the velocity $\dot{\mathbf{p}}$ of a point of the platform and its angular velocity $\boldsymbol{\omega}$. The transformation matrix

$$\mathrm{J}=\begin{pmatrix}\mathbf{q}_{1,1} & \mathbf{f}_{1,1}+\mathbf{PC}_1\times\mathbf{q}_{1,1}\\ \vdots & \vdots\\ \mathbf{q}_{3,2} & \mathbf{f}_{3,2}+\mathbf{PC}_3\times\mathbf{q}_{3,2}\end{pmatrix} \tag{19}$$

it called the Jacobian matrix.

In [30], the kinematic-static duality is proven. The Jacobian matrix that relates the velocity, also expresses the relation between the forces $\tau_{i,j}$ (i=1,2,3 and j=1,2 so that $\boldsymbol{\tau}=[\tau_{1,1}\ ,\ ..\ ,\ \tau_{3,2}]$) exerted by the actuators and the correspondent wrench $\mathbf{W}=[\ \mathbf{F}_p\ \mathbf{M}_p]$ generated on the platform ($\mathbf{F}_p$ is the force applied on the centroid of the platform and $\mathbf{M}_p$ is the moment applied on the platform) as follows:

$$J^T\boldsymbol{\tau} = \mathbf{W} \tag{20}$$

For the application for which the manipulator is used, the inverse relation takes on a greater interest:

$$\boldsymbol{\tau} = J^{-T}\mathbf{W} \tag{21}$$

since for a given value of the flexion angle the wrench **W** applied on the tibia is known.

The static analysis conducted for the dimensioning procedure consists of simulating the behavior of the manipulator under loading conditions that are going to be replicated during the in vitro tests. In particular, the loads to which the human joints are subjected during daily life and sport activities are considered. Their maximum values ([4-7]), can be resumed as follows (the values are given with respect to the fixed reference system S_B):

- ±1000 N along X and Y axes;
- ±3000 N along Z axis;
- ±200 Nm about X, Y and Z axes.

The wrenches used for the simulation are all the 64 combinations obtained considering the maximum values of forces and moments. The forces exerted by the actuators to replicate these wrenches are evaluated for several configurations of the manipulator. In particular, the set of 125 orientations of the platform given by all the combinations of the following values of the angles η, φ and ψ are examined:

- η evaluate for 0°, ±5°, ±10°;
- φ evaluate for 0°, ±15°, ±30°;
- ψ evaluate for 0°, ±15°, ±30°.

This set of orientations is the same that is used also for the workspace and singularity analyses.

Moreover, the simulation is conducted for some positions of the centroid of the platform. In particular, the 27 points obtained as all the combinations of the following value of the Cartesian coordinates x, y and z with respect to S_B, are considered:

- x evaluate for 0, ±0.01 m;
- y evaluate for 0, ±0.04 m;
- z evaluate for 0.8853 m, 0.8853±0.04 m.

These z values are defined during the workspace analysis and their definition is explained in the next chapter. For sake of clarity, it is anticipated that the centroid of the workspace of the manipulator is defined by the point [0 0 0.8853].

A total of 216000 (64·125·27) cases are analyzed and the maximum value of the force obtained for the chosen geometry is 7300 N.

CHAPTER 4 – WORKSPACE ANALYSIS

Introduction

In this chapter the numerical workspace analysis is reported. In general, the determination of the workspace for a spatial parallel manipulator with six DOFs is not an easy task. The visualization of the workspace is not possible: for a six DOFs parallel manipulator a workspace visualization is possible only if three out of the six DOFs are fixed.

Different types of workspace are defined, once the fixed parameters are chosen:

- *fixed orientation workspace*: all the possible locations that can be reached by a reference point of the platform with a given orientation;
- *fixed pose workspace*: all the possible rotations that the platform can achieve, given the position of the reference point;
- *maximum workspace*: all the possible location that the reference point of the platform can reach with at least one orientation;
- *dexterous workspace*: all the locations that the reference point of the platform can reach with a given set of rotations of the platform.

Workspace of parallel robot can be obtained with several method, depending on the type of wanted workspace. They can be grouped in:

1. Discretization methods: [31-33] are the simplest method to determine the workspace of a parallel manipulator. Several types of discretization methods were presented in literature. The most immediate one discretizes a large enough rectangular space along the Cartesian directions to form a regular cluster of points. For each point the inverse kinematics is solved, and the considered constraints are checked. Usually, the maximum and minimum length of the actuators, possible collisions between the links and limits of the passive joints are considered.

   The most efficient discretization method aims at computing the workspace boundary [32]: from an arbitrary point within the workspace, some searching directions in a spherical coordinate system (identified discretizing the range of azimuth and zenith angles) are analyzed in order to find the point, along that direction, in which the constraints are no longer respected.

Other methods find the workspace fixing four of the six DOFs to get planar cross-sections [33].

These methods have the great advantage to be easily adapted to all the robot architectures once some constraints are established. On the other hand, they require a very high computational cost and the shape of the workspace obtained is not precise.

2. More elaborate numerical methods for computing the boundary of the workspace have been developed [34]. All of them use analytical conditions that are solved numerically. In [35] the implicit function theorem is used to define singular configurations of mechanisms as criteria for boundaries of workspaces. Analytical conditions associated with the geometry of specific manipulators have been used by a number of authors to obtain explicit criteria for boundaries of workspaces [36-39]. These methods are very complex and do not solve the problem of the poor accuracy on the shape of the boundary.
3. Gosselin [40] developed an algorithm for finding the boundary based on a geometrical modeling of the constraints limiting the workspace (only the maximum and minimum elongation were considered in the computation). Subsequently, Merlet [41] extend the algorithm including also other constraints. This method can achieve an exact result but is not easily adaptable to all the manipulator and heavily depends on the constrained considered.

In this work, a discretization method is used. Indeed, a precise shape of the workspace is not required since the objective is to verify that the workspace is large enough to contain the functioning workspace required by the loading system during the in vitro tests.

The workspace analysis, described in this chapter, aims at computing the dexterous workspace as the intersections of some fixed orientation workspaces, the same orientation used for the static analysis.

Computation of a fixed orientation workspace

Fixed orientation workspace is defined as the space in which, a reference point of the platform can move, given a specific orientation of the platform. The orientation of the platform is defined by the transformation matrix ${}^{b}\mathbf{R}_{p}$ (as in relation (2)).

When a fixed orientation workspace is under evaluation, the value of the angles η, φ and ψ is given, and the aim is to find the space that the point P (the centroid of the platform Fig. 2.2) can reach. The constrains considered for the computation of the fixed orientation workspace are given by:

1. the maximum and minimum elongation of the prismatic joints: the electro-cylinder actuators length plus a loads cell and some components needed for the

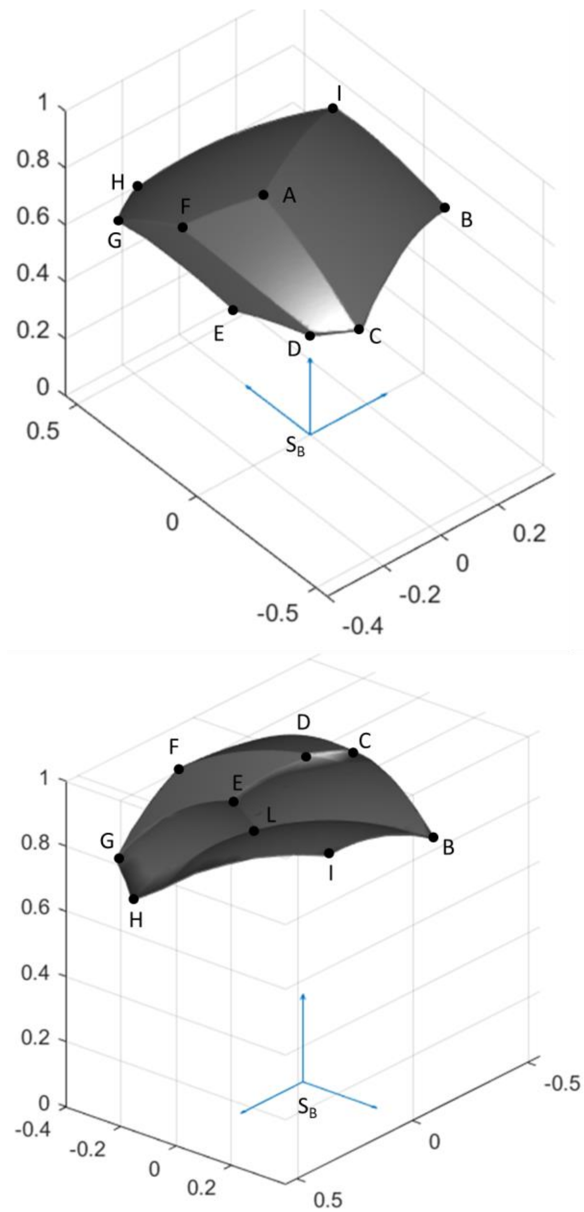

Figure 4.1. Fixed orientation workspace with η = 0°, φ = 0° and ψ = 30°.

connection (namely the segment $A_{i,j}B_{i,j}$) can vary from 783mm to 1073mm.

2. possible collisions between the load cells belonging to the same kinematic chain.

No check is included on singular conditions of the manipulator and on the mobility of the passive joints.

Figure 4.1 shows the workspace of the manipulator when the orientation of the matrix is defined by the following values of the angles: $\eta = 0°$, $\varphi = 0°$ and $\psi = 30°$.

For example, when the manipulator reaches the position corresponding to the point D, the configuration is that the actuator corresponding to the segment $A_{2,2}B_{2,2}$ reaches its maximum elongation (Fig. 4.2).

Workspace boundary was determined with a method similar to [32]. 3600 equally spaced searching directions in a spherical coordinate system are considered. The determination of the boundary point along a specific direction is found using the Bisection method. Along that specific direction a function that is 1 if the constrains are met and -1 if they

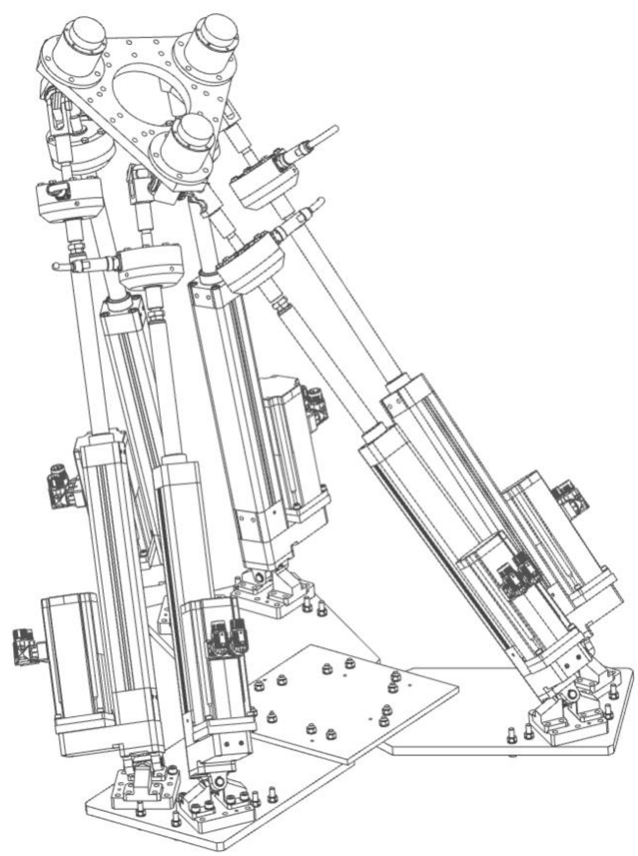

Figure 4.2. Fixed orientation workspace with $\eta = 0°$, $\varphi = 30°$ and $\psi = 0°$.

are not, is evaluated. Each searching direction has its starting point coinciding with the position in which the centroid of the mobile platform is located when all the actuators have an elongation of half of the stroke.

Computation of a specific dexterous workspace

The dexterous workspace of a six-DOF manipulator can be computed as the common space between a set of fixed orientations workspace.

As mentioned in the third chapter, a set of 125 orientations of platform is considered, and, consequently, 125 fixed orientation workspaces are computed. The intersection between all of them is shown in Fig. 4.3 and Fig. 4.4. The envelope of the workspace can be described by means of some extreme points, which coordinates are shown in Table 4.1, and its volume is $5.2107 \cdot 10^{-3}$ m^3.

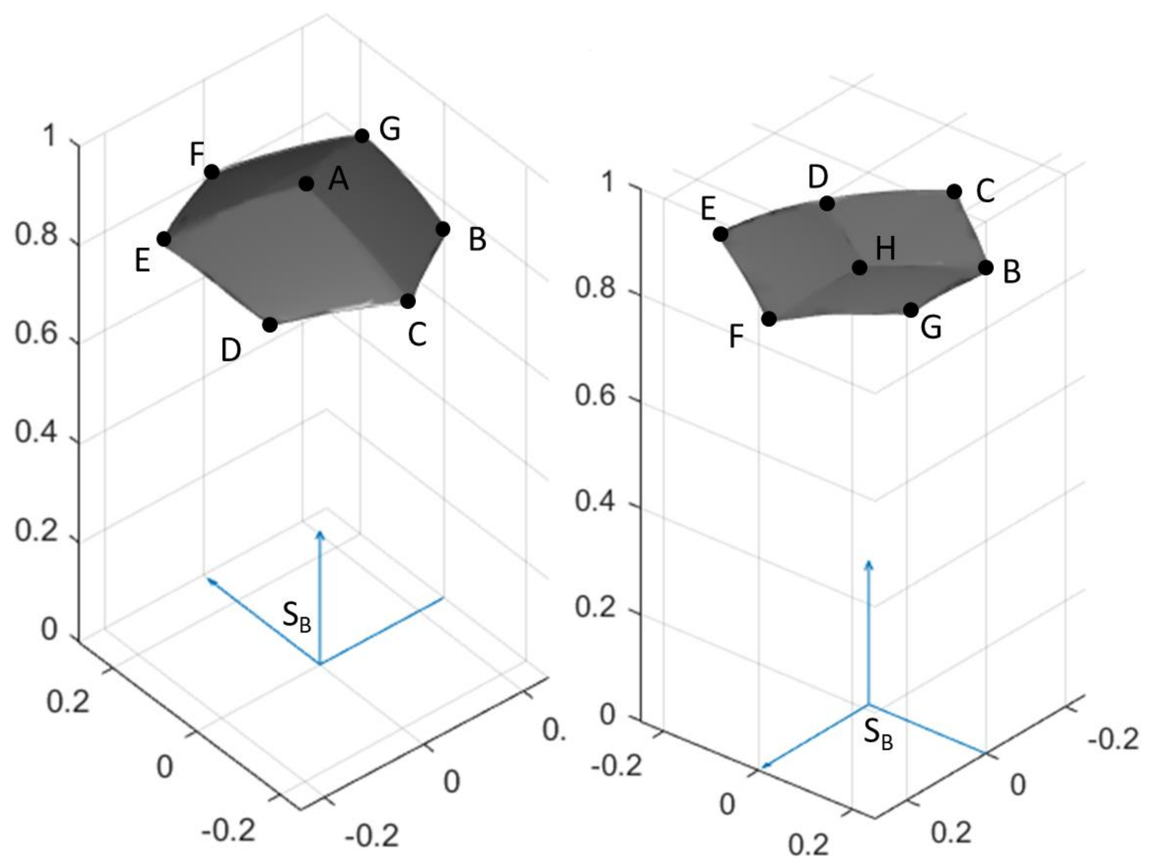

Figure 4.3. Dexterous workspace.

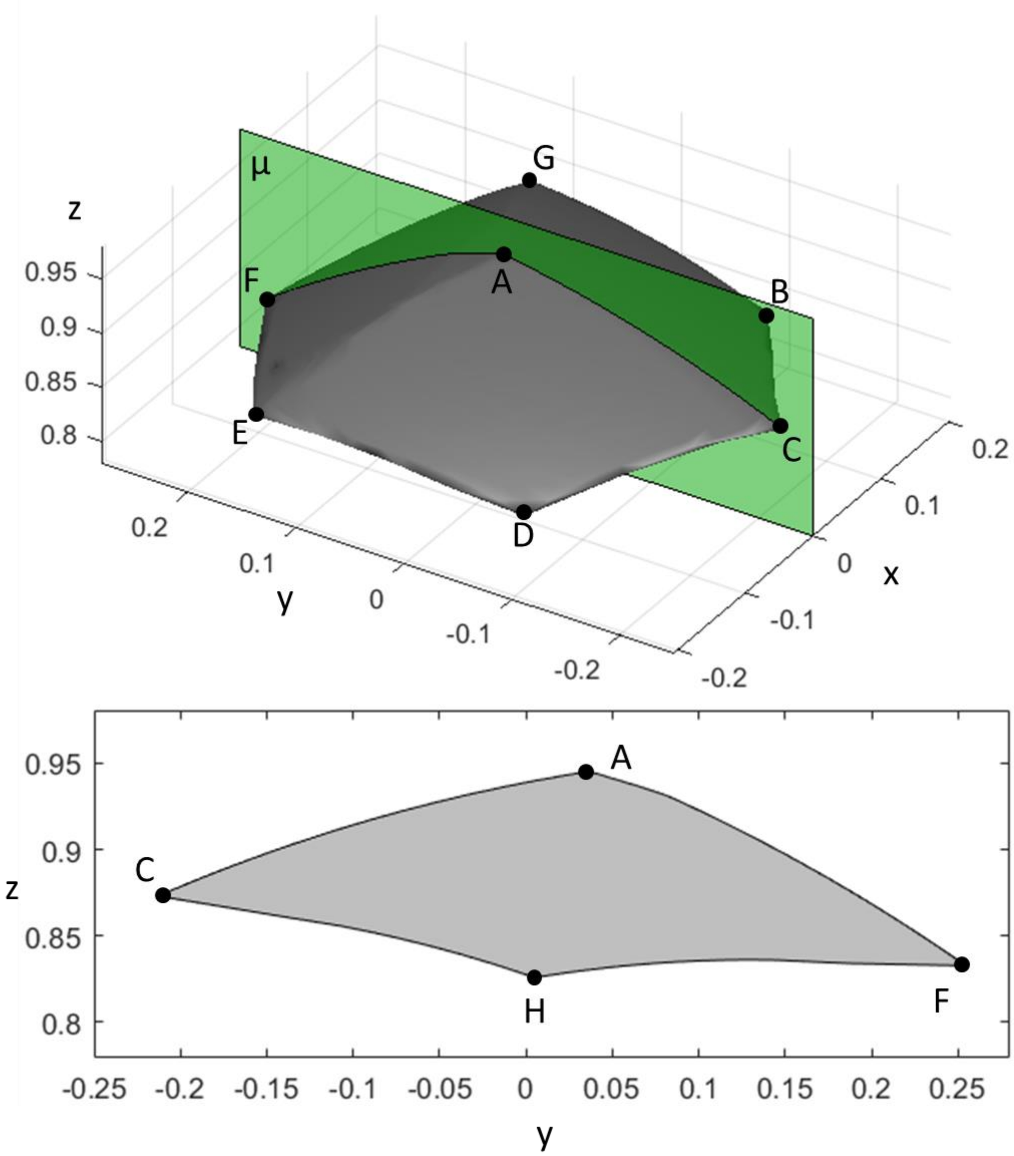

Figure 4.4. Section of the dexterous workspace on the plane μ (green).

Points	x	y	z
A	0	0.0375	0.9447
B	0.1752	-0.091	0.8451
C	0	-0.2155	0.8701
D	-0.1752	-0.091	0.8451
E	-0.2067	0.1371	0.871
F	0	0.2592	0.8274
G	0.2067	0.1371	0.871
H	0	0.0047	0.8259

Table 4.1. Position of the extreme points of the workspace with respect to S_B (dimensions are in m).

Conclusion

The needed operating space, which dimensions are described in the second chapter, is abundantly enclosed on the dexterous workspace of the manipulator.

The red parallelepiped shown in Fig 4.5 (defined by the points V_n, n = 1, … ,8) that represents the needed workspace has a volume of $1.28 \cdot 10^{-4}$ m^3. It is possible to define a general index R_V to express a relation between the two spaces using the ratio between their volumes:

$$R_V = \frac{workspace\ volume}{needed\ space\ volume} = \frac{5.2107 \cdot 10{-}3\ m^3}{1.28 \cdot 10{-}4\ \ m^3} = 4.1 \tag{22}$$

If the index is bigger than 1, the dexterous workspace is bigger than the needed workspace. R_V is obviously a purely indicative index, and, thus, when it is bigger than 1 another method is used to verify the result and consists of the following procedure:

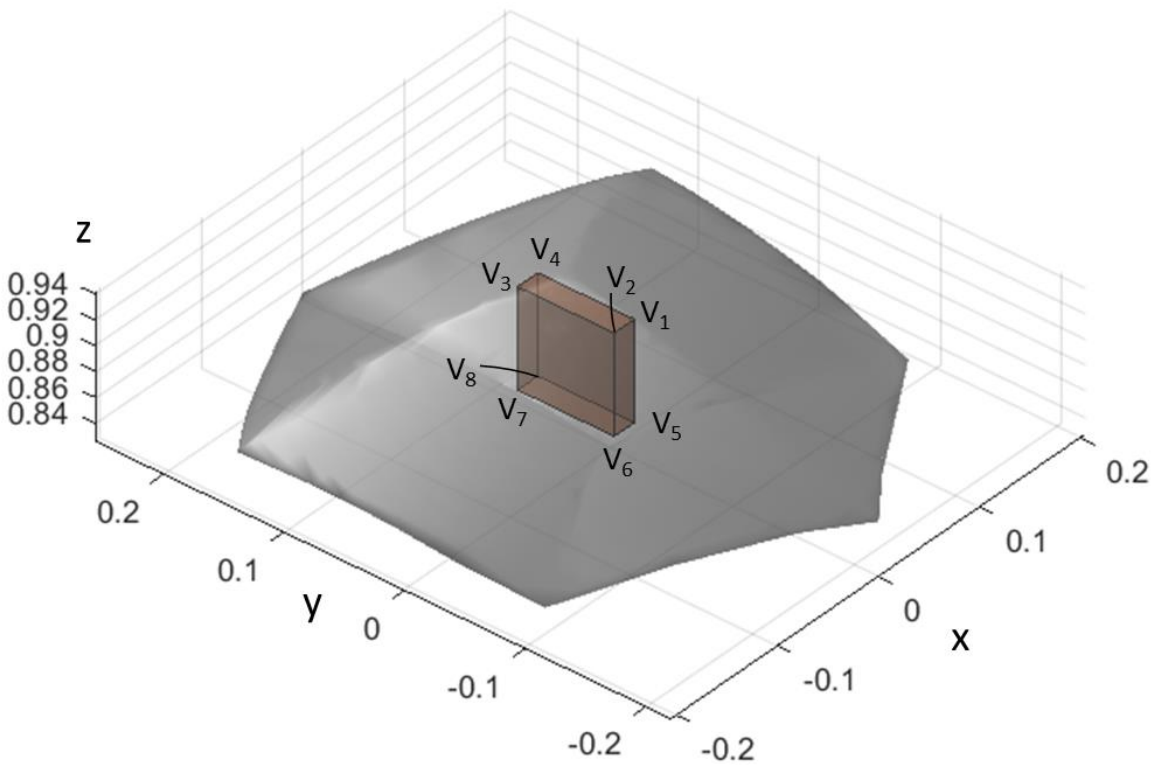

Figure 4.5. Required functioning space (red) abundantly enclose on the dexterous workspace.

1. the needed operating workspace centroid V_9 is positioned in along the Z-axis of S_B, at a height that is the average between the z-coordinate values of the points A and H. Accordingly, the position of the vertices V_n (n = 1, ... ,8) is determined (Table 4.2).
2. the intersection of the dexterous workspace with the two planes passing through the superior (V_1, V_2, V_3 and V_4) and inferior (V_5, V_6, V_7 and V_8) vertices of the parallelepiped, is determined. In particular, two curves (black in Fig. 4.6) are obtained, one for each plane.
3. check is made if rectangles V_1, V_2, V_3 and V_4, and V_5, V_6, V_7 and V_8 (red in Fig. 4.6) are completely enclosed within the respective curve.

For the geometry of the manipulators no intersections occur between the two spaces.

Points	x	y	z
V_1	0.010	-0.040	0.9253
V_2	-0.010	-0.040	0.9253
V_3	-0.010	0.040	0.9253
V_4	0.010	0.040	0.9253
V_5	0.010	-0.040	0.8453
V_6	-0.010	-0.040	0.8453
V_7	-0.010	0.040	0.8453
V_8	0.010	0.040	0.8453
V_9	0	0	0.8853

Table 4.2. Position of the vertices of the needed space with respect to S_B (dimension expressed in m). V_9 is the centroid of the needed space.

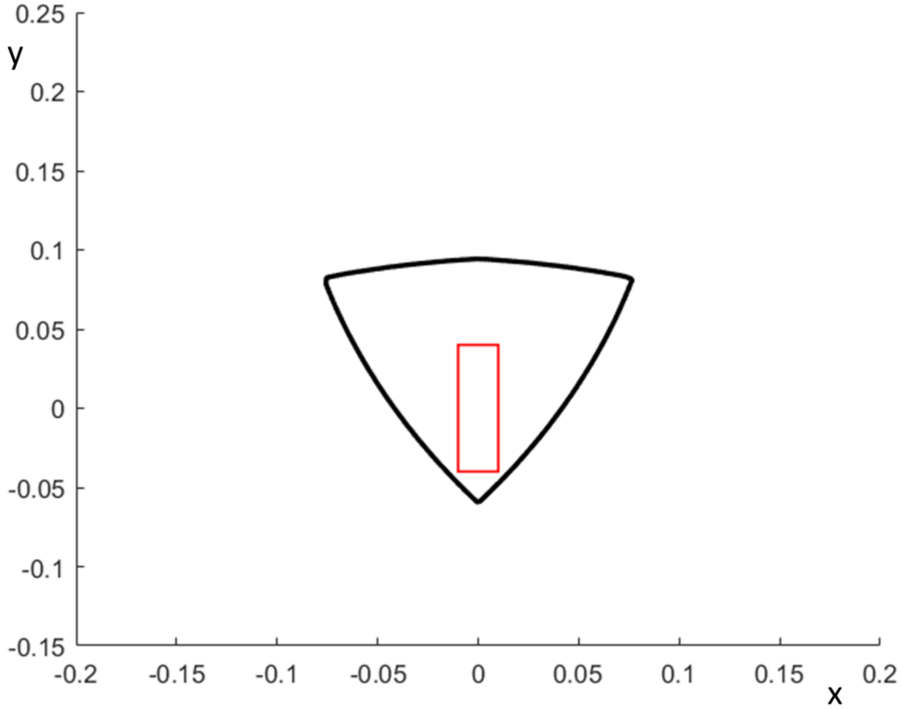

a)

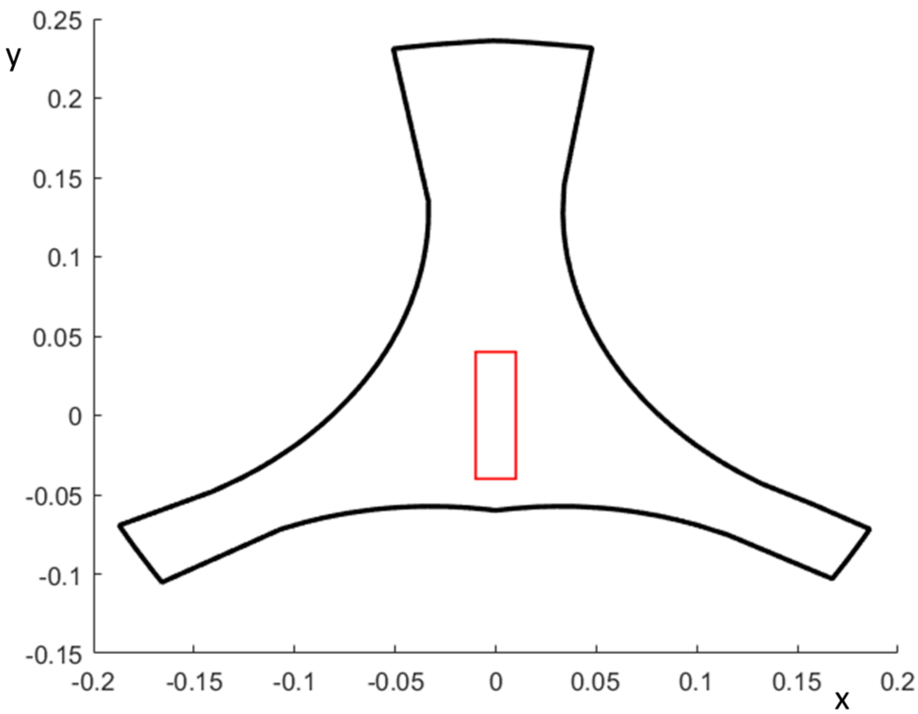

b)

Figure 4.6. Cross-section of the workspaces on a plane passing through the points V_1, V_2, V_3 and V_4; b) Cross-section of the workspaces on a plane passing through the points V_5, V_6, V_7 and V_8.

CHAPTER 5 – SINGULARITY ANALYSIS

Introduction

From a mathematical point of view, singular configurations are those configurations in which the determinant of the Jacobian matrix (relation (19)) associated to the manipulator becomes zero. Equivalently, with reference to the relation (18), a singular configuration occurs when, even though the actuators are locked (and, thus, the joint velocity $\dot{l}_{i,j}$ are equal zero), the vector $[\dot{\mathbf{p}}^{\boldsymbol{T}}\ \boldsymbol{\omega}^{\boldsymbol{T}}]^{\boldsymbol{T}}$ is not zero.

When a singularity occurs, the manipulator gains one or more degrees of freedom and, thus, it is no more controllable. Moreover, in a singular configuration, for any wanted wrench **W** on the platform , the forces exerted by the actuators tend, theoretically, to infinity. Thus, the value of the forces is still very high near a singularity, and this could lead to the rupture of the components of the manipulator. Therefore, it is not only important to detect the singularities to avoid them, but also to operate far from them.

That explains why the study of the singularity conditions is so important and why the literature is full of papers that describe methods and procedures to detect them.

In the literature several methods that aim at geometrically determining the singular configurations are presented. The most important is the method proposed by Merlet in [42]. He uses Caley-Grassman Algebra to detect the singular configurations of the 6-3 GS platform. Then, other authors extend this method to general case [43, 44]. In his work, Merlet approaches the study from a static point of view, showing that each row of the Jacobian matrix identifies a constraint on the platform (in this case is a force). Each one of the constraints can be expressed by a Plücker coordinate (thus, by a line). therefore, the Jacobian matrix can be examined considering six lines. Moreover, Merlet makes a list of some possible conditions that generate the linear dependency of one or more lines with respect to the other.

In this work, the Jacobian matrix related to the new manipulator, obtained from the kinematic analysis, cannot be treated in the same way, since its rows are not representative of Plücker coordinates.

Therefore, a numerical method is used to find the singular configurations of the manipulator.
As a matter of fact, exploiting a characteristic of the kinematic chain, it is possible to obtain a new Jacobian matrix whose rows are representative of Plücker coordinates. That allows the characterization of the singularity obtained from the numerical analysis by means of the Caley-Grassman Algebra.

Numerical singularity analysis

A procedure similar to the one used for the workspace analysis is used for singularity analysis. Indeed, a fixed orientation singular surface can be defined as the surface that, given a specific orientation of the platform, identifies the positions of the reference point of the platform in which the Jacobian matrix becomes singular. The orientation of the platform is defined the same way as it is done for the fixed orientation workspace. Also, the same method used to define the workspace boundary is adopted here: in particular, the Bisection method is used to find when the determinant of the Jacobian matrix is zero along the same 3600 directions.
Fig. 5.1 shows the fixed orientation singular surface (blue) and the fixed orientation workspace (gray, the same as Fig. 3.1) defined by the following angles: $\eta = 0°$, $\varphi = 0°$ and $\psi = 30°$. The figure shows the zone of the singular surface near to the workspace. A more detailed image of the singularity surface is shown in appendix A.3.
A total singular surface can be defined as the points belonging to a set of fixed orientation singular surfaces, nearer to a point of the dexterous workspace (in this case it is defined as the position of the centroid when the actuators have an elongation of half of the stroke) along some searching directions. The same directions used for the computation of the fixed orientation singular surfaces are used in the computation of total singular surface.
For example, Figure 5.2 shows two singular surfaces defined by the values of the angle $\eta = 30°$, $\varphi = 0°$ and $\psi = 0°$ (red, in Appendix A.3 a more detailed image of the singular surface is shown) and $\eta = 0°$, $\varphi = 0°$ and $\psi = 30°$ (green). The black lines in the figure identify two searching directions k_1 and k_2, that meet the singular surfaces in four points I_1, I_2, I_3 and I_4 (I_2 and I_3 are on the first surface, I_1 and I_4 are on the second surface). In this case, the point I_2 belonging to the first fixed orientation singular surface is nearer to

the considered point O along the direction k_2, whereas the point I_1 is nearer along the direction k_1. Repeating the computation for some directions it is possible to find all the nearer points. Thus, the total singular surface related to the set of these two fixed orientations can be computed.

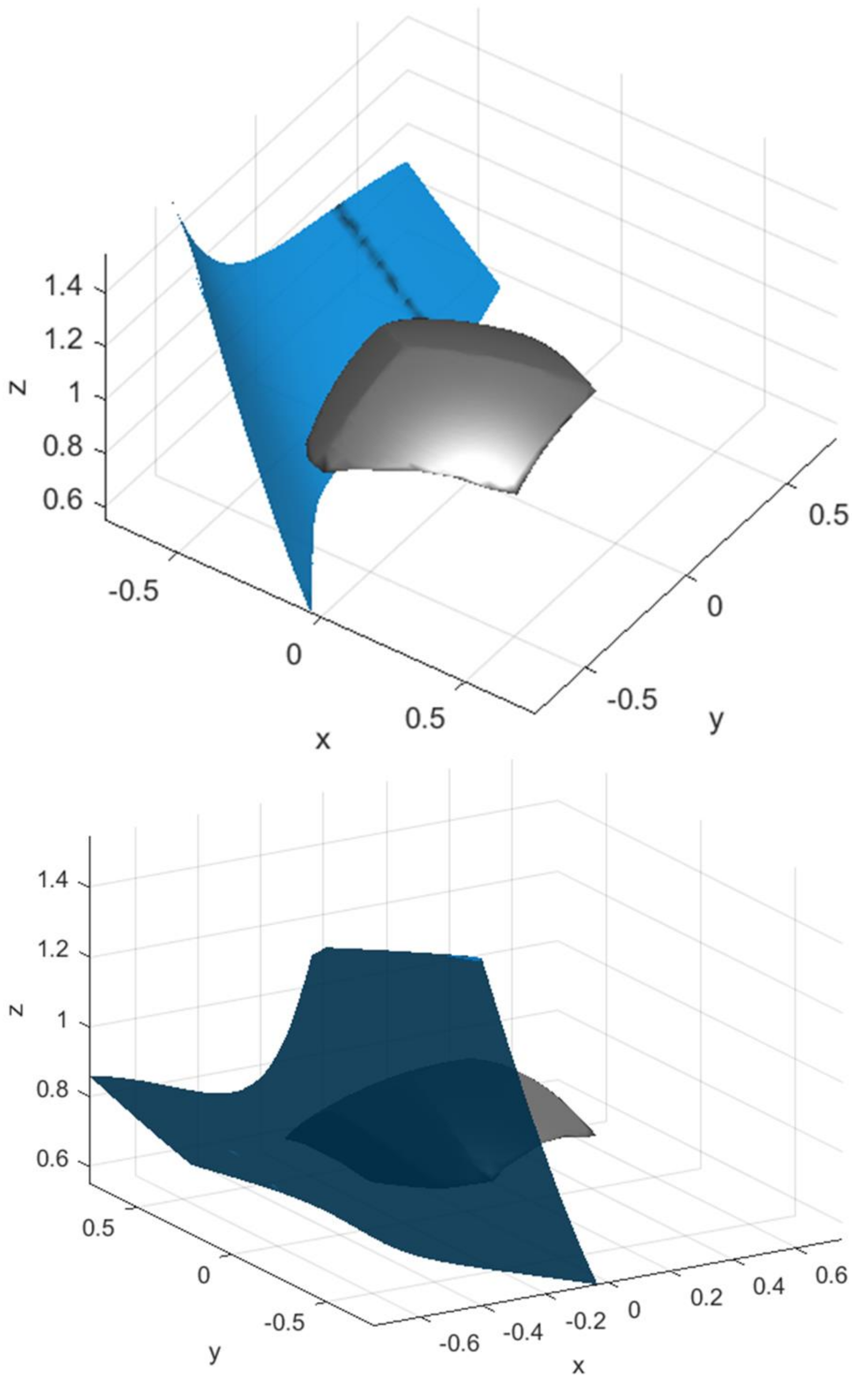

Fig. 5.1. Fixed orientation singular surface (blue) and workspace (gray) with $\eta = 0°$, $\varphi = 0°$ and $\psi = 30°$.

Fixed oriented singular surfaces are computed for the same 125 orientations of the mobile platform used previously. From them, the total singular surface is obtained and shown in Figure. 5.3.

As shown in Figure 5.3, the total singular surface abundantly encloses the dexterous workspace that, thus, is free from the singularities associated to the same orientations of the platform.

Characterization of the singularity

For the sake of clarity, the Jacobian matrix (19) is repeated:

$$\mathrm{J} = \begin{pmatrix} \mathbf{q}_{1,1} & \mathbf{f}_{1,1} + \mathbf{PC}_1 \times \mathbf{q}_{1,1} \\ \vdots & \vdots \\ \mathbf{q}_{3,2} & \mathbf{f}_{3,2} + \mathbf{PC}_3 \times \mathbf{q}_{3,2} \end{pmatrix} \tag{23}$$

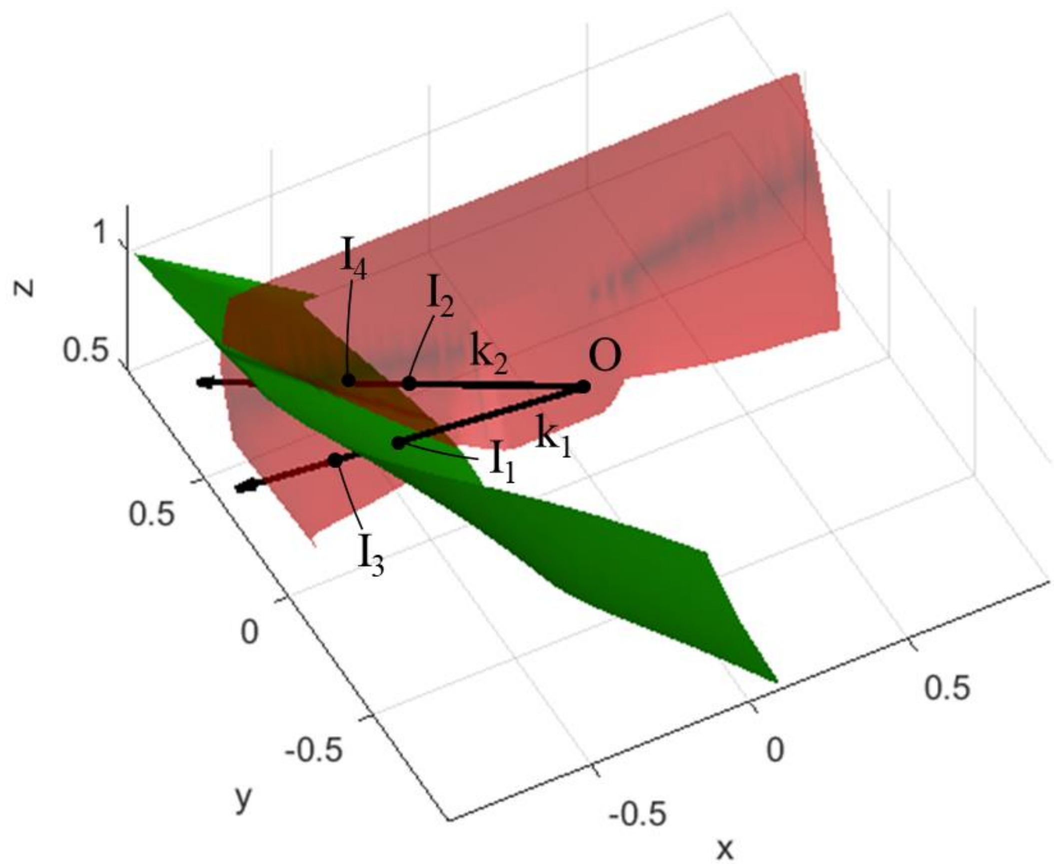

Fig. 5.2. Identification of the total singular surface.

As mentioned before, each column of $\mathbf{J}^T$ doesn't express a Plücker coordinate since the term $\mathbf{f}_{i,j}$ is not orthogonal, in general, to $\mathbf{q}_{i,j}$, thereby, the Jacobian matrix can't be used to

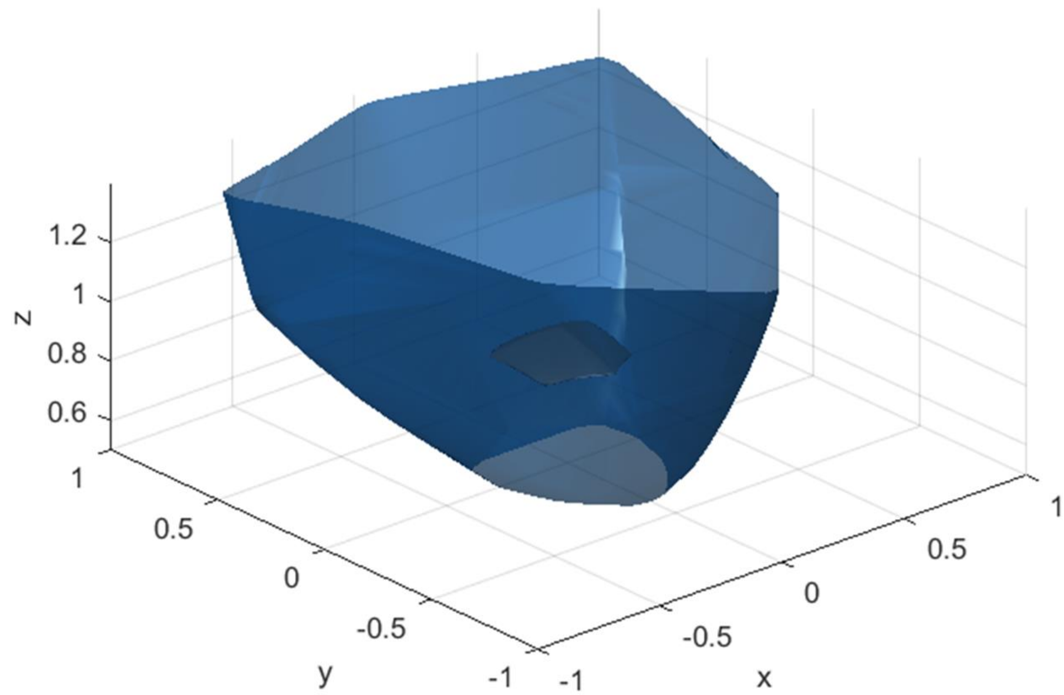

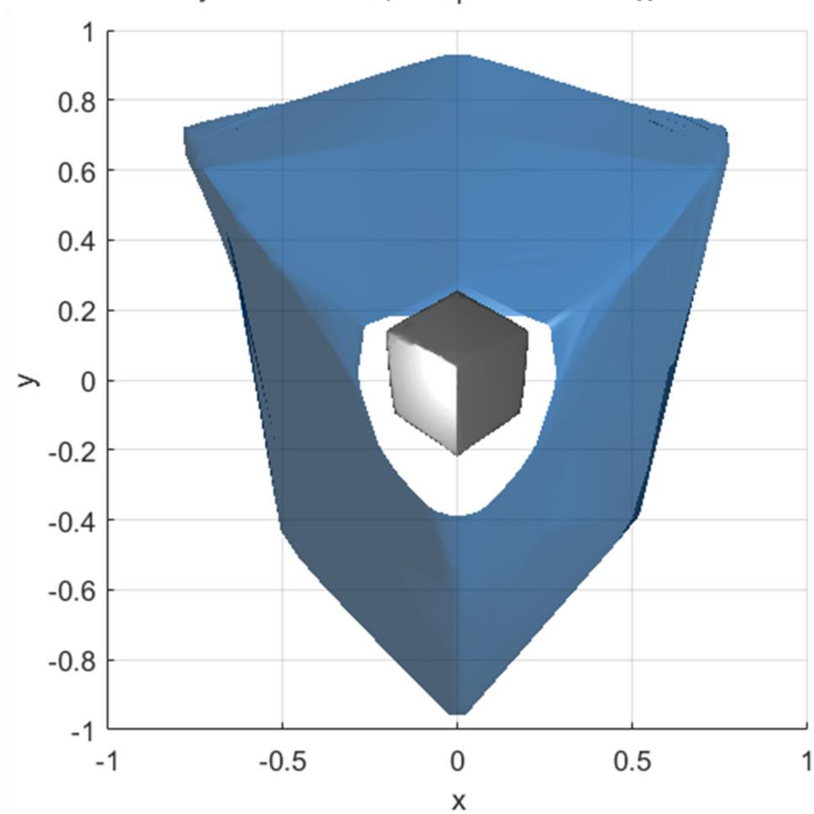

Fig. 5.3. Total singular surface (blue) and dexterous workspace (gray).

study geometrically the singular configurations of the new manipulator according to the method proposed by Merlet.

However, it is always possible for each kinematic chain to find the relative constraints that each one applies on the platform (in particular 2 constraints have to be found since, when the actuators are locked, each kinematic chain has 4 DOFs). If these constraints can be expressed in terms of equivalent forces the abovementioned method can be used.

As a matter of fact, two forces can be found for each kinematic chain. Indeed, if the actuators are locked, each kinematic chain is equivalent to a serial 4 DOFs chain composed by 4 revolute joints: the first R joint axis is coincident with the line passing through $A_{i,1}$ with direction $\mathbf{r}_i$ (line $\mathbf{M}_i$), the second R joint axis is coincident with a line passing through the point D_i (that is the meeting point of the lines passing through the

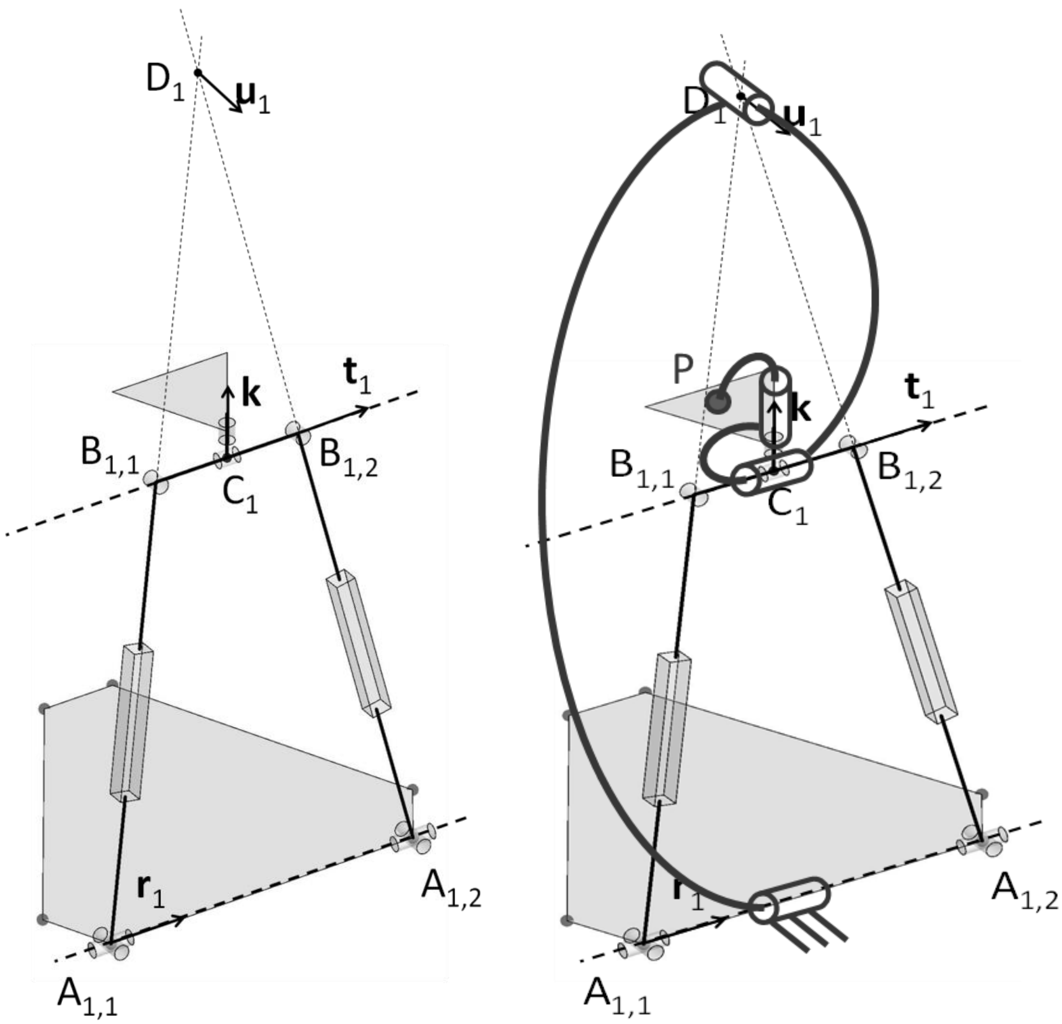

Fig. 5.4. Representation of the first kinematic chain as a serial link with 4 R joints.

points $A_{i,1}$ and $B_{i,1}$and the points $A_{i,2}$ and $B_{i,2}$ respectively) with direction $\mathbf{u}_i$ (line $\mathbf{U}_i$), the third and the fourth R joint axes are coincident with the line passing through C_i with direction $\mathbf{t}_i$ and $\mathbf{k}$ respectively (lines $\mathbf{T}_i$ and $\mathbf{K}$) (Fig.5.4).

It is possible to find a line, $\mathbf{L}_{i,1}$, passing through the R joint axes of the serial chain, since a line passing though D_i and C_i (and thus, the second, third and fourth R joints) always meets the axis of the first R joint, since D_i, C_i and $\mathbf{M}_i$ lie on the same plane γ_i (Fig.5.5-a).

The second constraint $\mathbf{L}_{i,2}$ line can be found depending on the configuration. Two cases may occur:

1. if $\mathbf{r}_i$ and $\mathbf{t}_i$ are not parallel (and thus meet in a point E_i, since they lay on the same plane), it is possible to find a line passing through the point E_i and intersecting lines $\mathbf{U}_i$ and $\mathbf{K}$ (Fig.5.5-b);

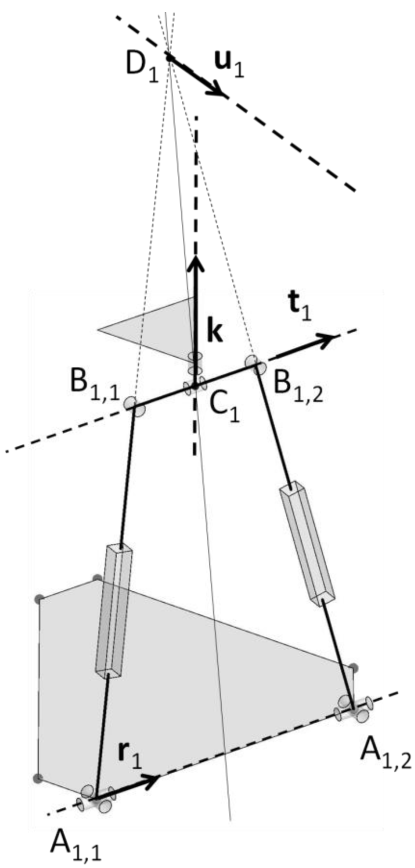

a)

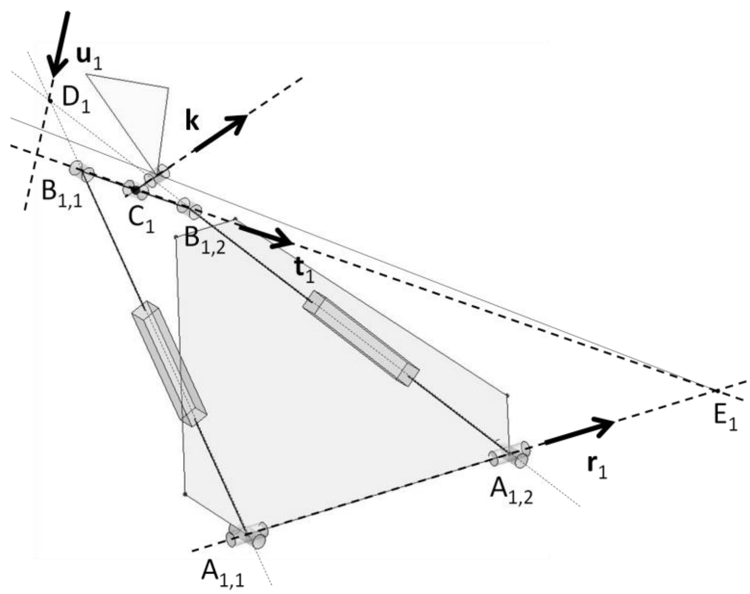

b)

Fig. 5.5. a) The first constraint is represented by the line (continuous) passing though D_i and C_i. b) The second constraint is represented by the line(continuous) passing though line $\mathbf{U}_i$, $\mathbf{K}$ and point E_i.

2. if $\mathbf{r}_i$ and $\mathbf{t}_i$ are parallel, it is always possible to find a line passing through $\mathbf{U}_i$ and $\mathbf{K}$ and parallel to $\mathbf{r}_i$ (and, thus $\mathbf{t}_i$).

A Jacobian based on the six constraints $\mathbf{L}_{i,j}$ (i=1,2,3; j=1,2, two for each kinematic chain) can be written, in which each row corresponds to a Plucker coordinate:

$$J = \begin{pmatrix} \boldsymbol{L}_{1,1} \\ \vdots \\ \boldsymbol{L}_{3,2} \end{pmatrix} \tag{24}$$

Thus, the singularities obtained from the numerical analysis can be studied according to the geometrical method [42]. 20 points uniformly distributed of the total workspace singularity surface are considered with the relative orientation.

In particular, two types of singular condition may occur (Fig. 5.6):

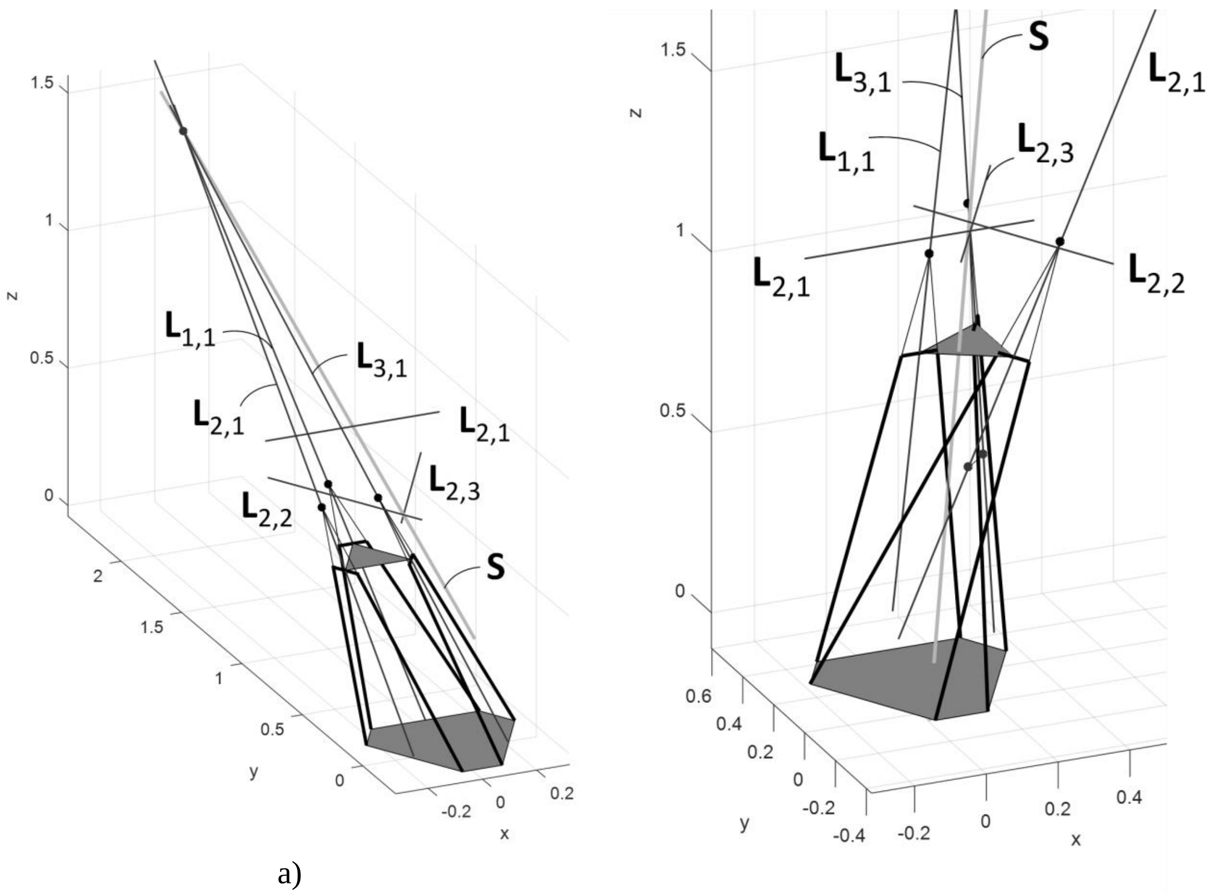

a) b)

Fig. 5.6. a) Singularity 5b: all the six line $\mathbf{L}_{i,j}$ meet the same line $\mathbf{S}$. b) Singularity 5a: the six line $\mathbf{L}_{i,j}$ belong to same linear general complex with screw $\mathbf{S}$.

1. 5b type singularity (all the lines meet a line, thus a rotation about that line is possible);
2. 5a type singularity (all the lines belong to the same general linear complex, thus an helicoidal motion is possible).

The singular surface corresponding to an orientation of the platform with angles $\eta=0°$, $\phi=0°$ and $\psi=0°$, coincides with a condition in which the six lines $\mathbf{L}_{i,j}$ meet the same line **S** (Fig.5.6-a) or five lines meet the same line **S** and the sixth line is parallel (or meets **S** at infinity), thus a rotation about **S** is possible (5b type singularity).

For the other orientations of the platform, the surfaces correspond to a condition (Fig.5.6-b) in which all the six lines $\mathbf{L}_{i,j}$, belong to the same linear general complex, thus an helicoidal motion of the platform with screw **S** is possible (type 5a singularity, a detailed characterization is described in [45]).

CHAPTER 6 – CONSTRUCTION

Design

This chapter deals with the mechanical design and construction of the manipulator. The design has been done with the use of the PTC Creo Parametric CAD software. Fig 6.1 shows the built manipulator.

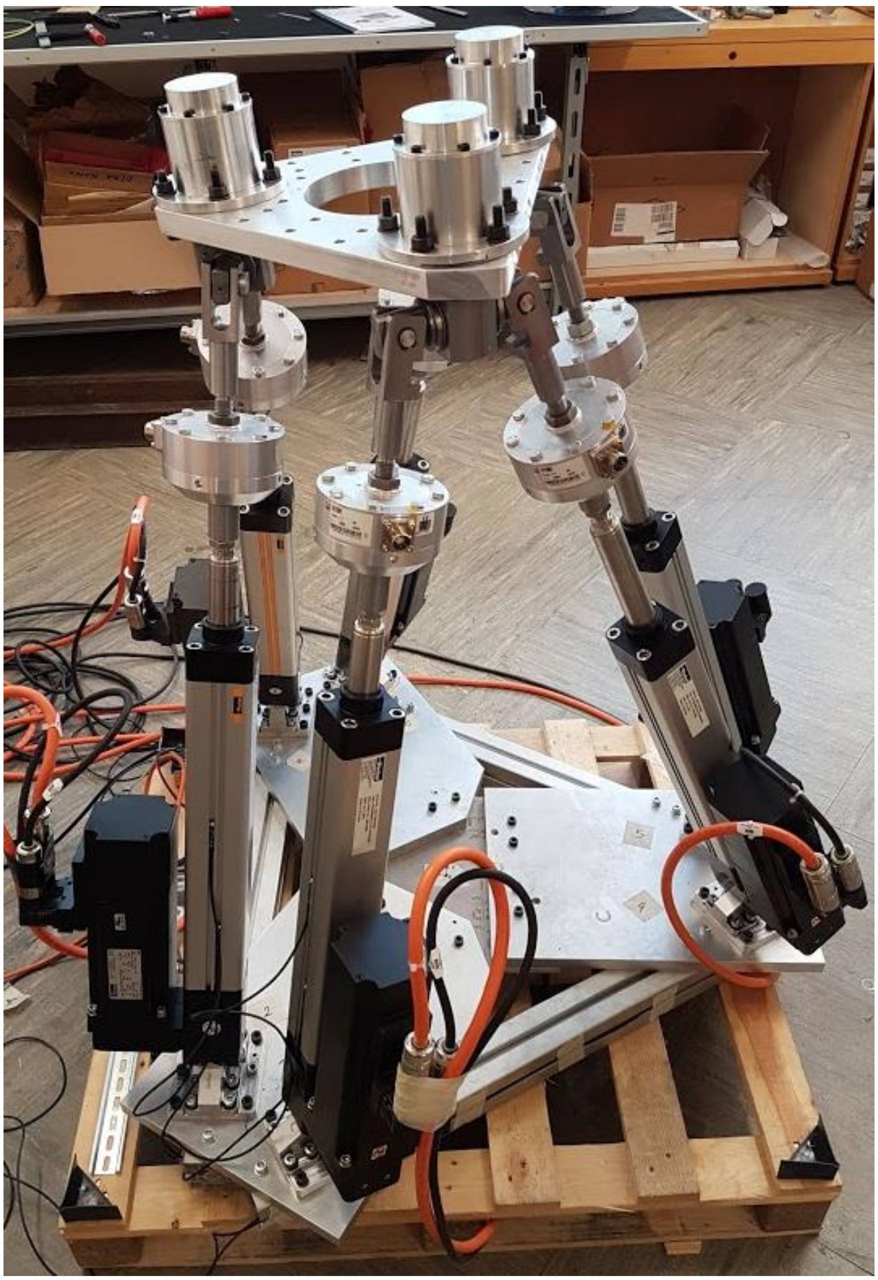

Fig. 6.1. The new manipulator.

Design and construction

As mentioned previously, the mobility of the passive joints is not considered as a constraint in the computation of the dexterous workspace because it is not known before the designing process. Indeed, once a geometry, and thus the dimensions d_p, d_b, φ_b and l is given, the mechanical dimensioning of the components of the manipulator is made based on the loads to which they are subjected to, on the geometry of the commercial components (they need to adapt to Parker electro-cylinder actuators and HBM load cells) and the capability of the machining at disposal.

If possible, the design process aims at realizing a manipulator which is not limited on passive joints: the dimensions and the shape of the elements are determined accordingly. Actually, the mobility of the passive joints obtained with the design leads to a dexterous workspace smaller than the previous one (the one in which the mobility of the passive joints is not considered).

Therefore, in order to understand if the new dexterous workspace is large enough to fulfil the required specifications, the passive joint mobility is analyzed.

In particular, the following quantities (Fig. 6.2) are analyzed:

$\theta_{i,j}$ that is the angle between the unit vectors $\mathbf{s}_{i,j}$and $\mathbf{v}_{ur,i}$, and is computed as

$$\theta_{i,1} = \text{acos}(\mathbf{s}_{i,1} \cdot \mathbf{r}_i);\ \text{for i} = 1,2,3; \tag{23}$$

$$\theta_{i,2} = \text{acos}(\mathbf{s}_{i,2} \cdot \mathbf{r}_i);\ \text{for i} = 1,2,3; \tag{24}$$

ξ_i that is the angle between the unit vectors $\mathbf{u}_i$and $\mathbf{v}_z$, and is computed as

$$\xi_i = 90° - \text{acos}(\mathbf{u}_i \cdot \mathbf{v}_z);\ \text{for i} = 1,2,3 \tag{25}$$

where $\mathbf{v}_z$ is the unit vector with direction along the Z-axis;

$\chi_{i,j}$ is the angle between the unit vectors $\mathbf{s}_{i,j}$and $\mathbf{v}_{ut,i}$, and is computed as:

$$\chi_{i,1} = \text{acos}(\mathbf{s}_{i,1} \cdot \mathbf{t}_i);\ \text{for i} = 1,2,3 \tag{26}$$

$$\chi_{i,2} = \text{acos}(\mathbf{s}_{i,2} \cdot \mathbf{t}_i);\ \text{for i} = 1,2,3 \tag{27}$$

The maximum value of the passive joint angles is obtained by mean of PTC Creo Parametric. The following constraints are used for the computation of the new dexterous workspace:

$$\theta_{i,1,min} = 61°;\ \theta_{i,2,max} = 119°;\ \xi_{i,max} = 115°;\ \xi_{i,min} = 75°; \chi_{i,1,max} = 120° \text{ and } \chi_{i,2,min} = 60°. \tag{28}$$

The Attachment A.4 shows the constructive solutions adopted to reach the required mobility of the joints. The volume of the workspace can be computed, and the index $R_{V,n}$ calculated:

$$R_{V,n} = \frac{workspace\ volume}{needed\ space\ volume} = \frac{3.668 \cdot 10{-}3\ m^3}{1.28 \cdot 10{-}4\ \ m^3} = 2.9 \tag{29}$$

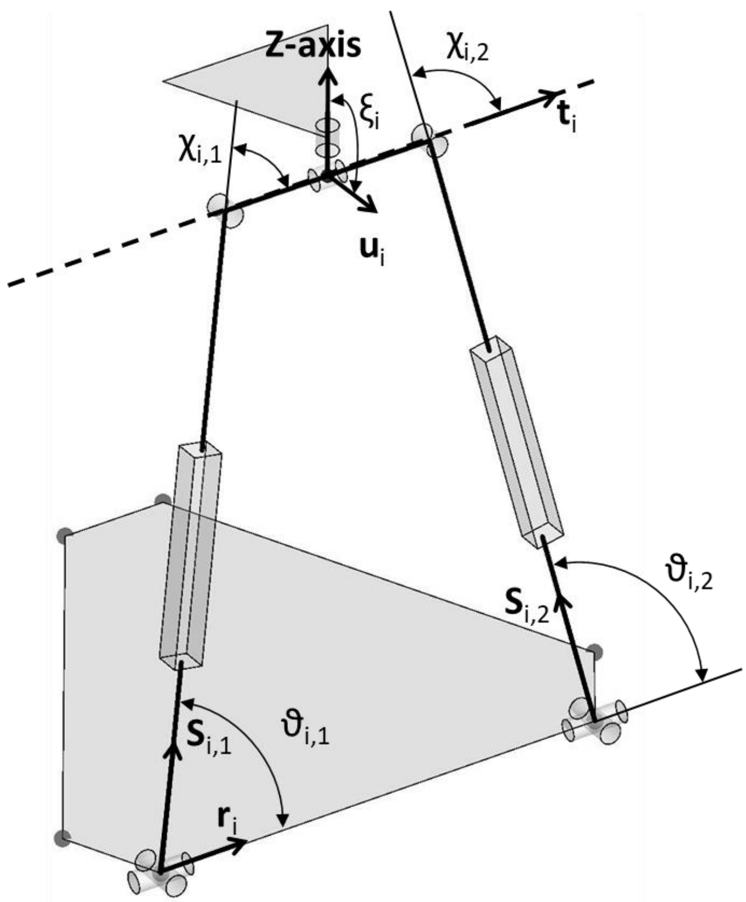

Figure 6.2. Graphical representation of the angles used for the computation of the passive joint mobility.

Figure 6.3 shows the graphical comparison between the two dexterous workspaces. The analysis conducted on the new workspace shows that it is smaller than the previous one ($\frac{R_{V,n}}{R_V} = \frac{2.9}{4.1} = 0.7$) but it is large enough to contain the needed workspace.

Electric components

For a complete description of the manipulator, the electric components used to build the position control system are listed below.

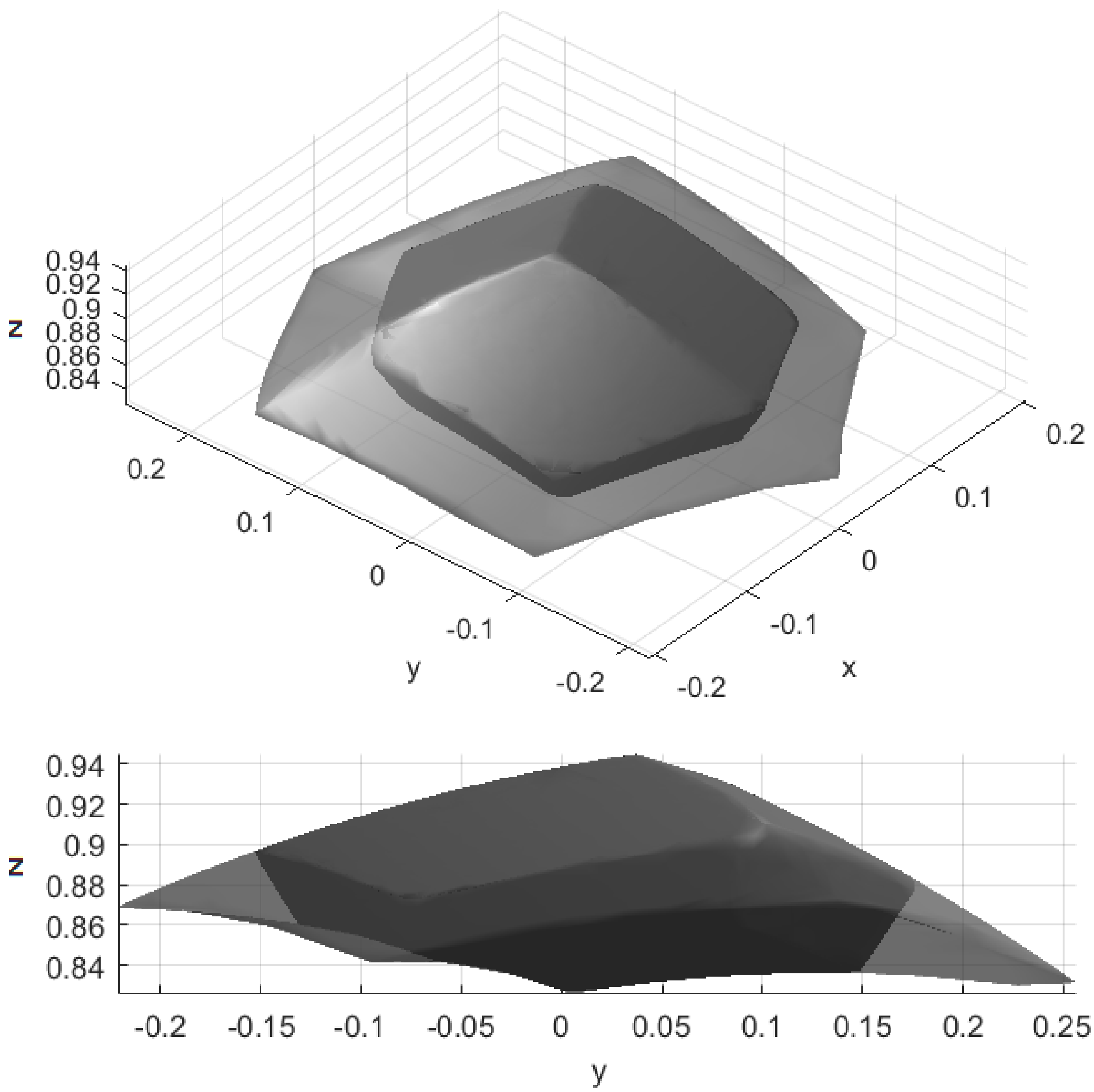

Figure 6.3. Comparison between the two dexterous workspaces.

CX 5120 – 0125 (Fig. 6.4) is an embedded-PC with an Intel Atom processor 1,46 GHz in which Microsoft Windows Embedded Standard 7 P (32-bit) is installed. The latter interfaces with TwinCAT 3 XAR installed on the PC. The connection of embedded-PC with the PC is done by an EtherNet cable.

Several Beckhoff modules can be connected to implement various digital or analog functions like, for example, the EL 1034 module, used to acquire the digital input signal of the limitations of the stroke.

SLVD-N (Small Low Voltage Drive - New) (Fig. 6.5-a) is a digital frequency converter for brushless motors. Its parameters can be easily configured with the operator interface and make the SLVD-N suitable for different applications.

It provides functions as a positioner with a trapezoidal profile, electrical shaft, electronic cams, spindle orientation, simulator of a step motor and torque control, and it also contains a PLC. It uses widely diffused industrial programming standards and guarantees a high degree of freedom in selecting inputs and outputs.

SMEA8230038142I65D52 is the brushless motor used to actuate the Parker ballscrew and its main characteristics are:

- Nominal torque: 2.7 Nm;
- Nominal velocity: 3000 rpm;
- Nominal current: 2.8 A;

Figure 6.4. CX 5120 – 0125 embedded-PC.

- Maximum torque: 9 Nm (4.8 Nm considering the driver);
- Inertia: 140 Kgmm^2;
- Absolute encoder HEIDENHAIN EQN1325.

The *EL1034* module (Figure 6.5-b) is a digital input terminal that acquires a 0-24V binary signal and makes it available on the EtherCAT bus. The module is provided with 4 isolated channels that are connected with superior and inferior limitation of the stroke sensors (two for each actuator, thus, each module can manage two actuators).

Figure 6.6 resumes schematically how the connection between the components just described is made.

a)

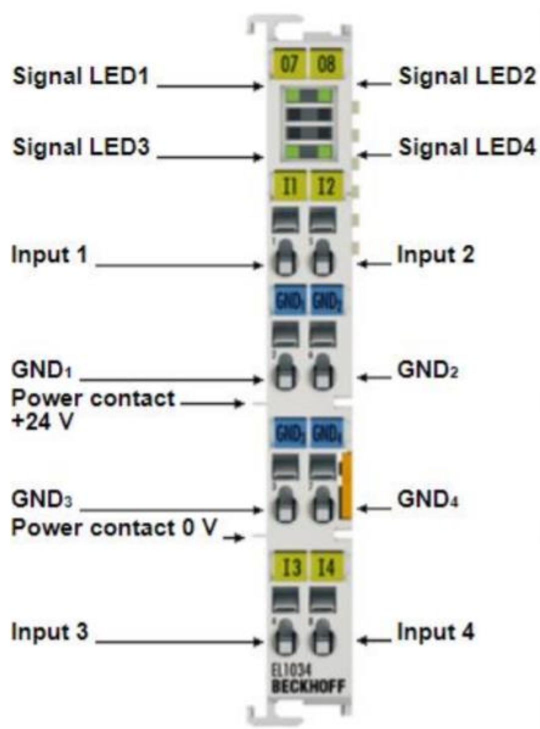

b)

Figure 6.5. a) SLVD-N; b) EL 1034 module.

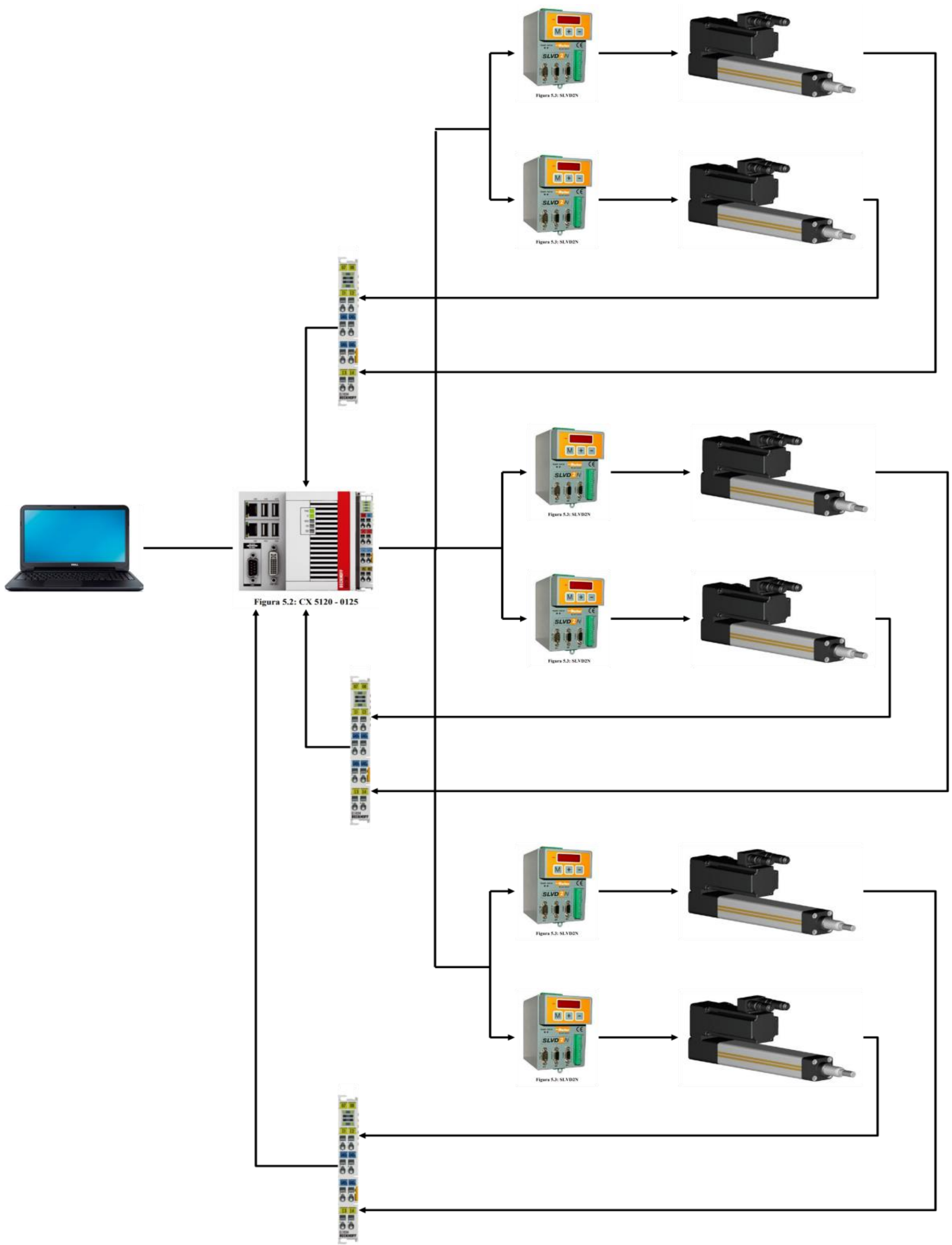

Fig. 6.6. schematic of the control system.

CHAPTER 7 – DISCUSSION AND CONCLUSIONS

The knowledge of the human joint behavior is essential for the design of protheses and for the validation of biomechanical models. In the last twenty years, many test rigs have been built with this purpose. Even though the Group of Robotics, Automation and articular Biomechanics (GRAB) of Bologna built a machine that proved to overcome the limitations of the previous machines, some improvements can still be brought to the rig.

This work presents the design and construction of a new six-DOF parallel manipulator to be used as the loading system in a new test rig, which can be seen as an evolution of the GRAB machine.

The new manipulator is a GS platform-based robot with some important features:

1. since it is 'overconstrained', it has a lower number of kinematic pairs with respect to other not overconstrained GS platforms. In particular, thrust bearings are avoided, simplifying the design process significantly,
2. it does not have spherical joints: spherical joints are known for their poor mobility unless bulky and expensive solutions are adopted,
3. particular connections ("pivot joints") between the actuators and the mobile platform are implemented that make it possible to have a workspace that is not affected by the presence of bulky, but high precision, load cells.

These characteristics provide the new manipulator with a high stiffness and high positioning accuracy.

Even though the manipulator, during the in vitro tests, is force controlled, the direct position analysis is used. Indeed, the load that must be applied is known for each flexion angle. In order to determine the vector of the forces on the actuators, also the Jacobian matrix is needed and, thus, the configuration of the platform. Therefore, positioning accuracy is required since the configuration is obtained by means of the absolute encoder of the brushless synchronous motors. Possible clearance in the joints of the kinematic chains would lead to a mistaken interpretation of the manipulator configuration. For being overconstrained, the new loading system is less affected by this kind of error with respect to other parallel architecture. Moreover, the manipulator shows a dexterous workspace (given a set of orientations of the platform) that contains the needed workspace and that is almost three times bigger. The dexterous workspace is free from

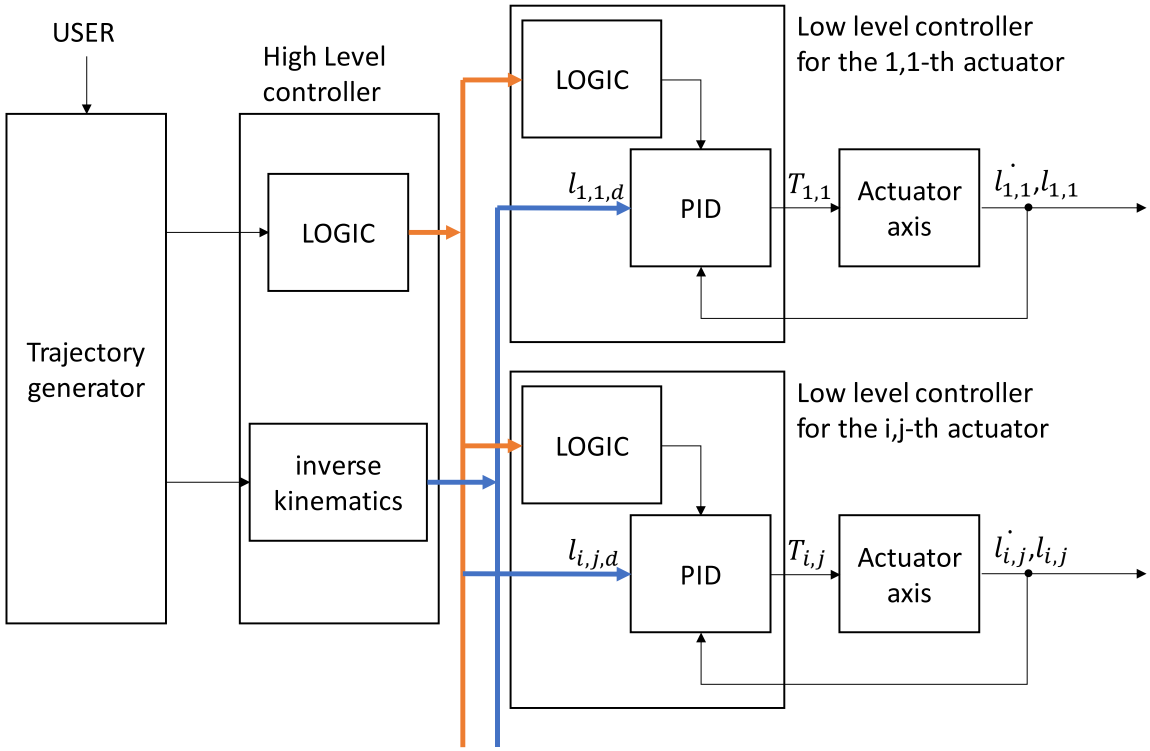

Fig. 7.1. Schematic of the position control loop.

singularity (for the same set of platform orientations used for computing the dexterous workspace). This characteristic is essential since the manipulator need to operate under force control.

All these features make the manipulator perfectly suitable as a loading system of the test rig.

Moreover, though the manipulator is designed to work for a particular application (in vitro tests) where the goal is to apply given loads to a specimen, the manipulator's characteristics are suitable also for all those applications, plenty in industrial automation, in which positioning accuracy is required. Generally speaking, given the dimensions of the mobile platform, a larger dexterous workspace can be reached keeping the dimension of the fixed base relatively small.

Tests were conducted on the manipulator under position control. In particular, the control architecture is a torque controlled system with position feedback: the motor torque $T_{i,j}$ is the manipulated variable in order to obtain the wanted length of i,j-th single axis. With reference to Fig 7.1, a low level controller implements a standard PID control law (in the

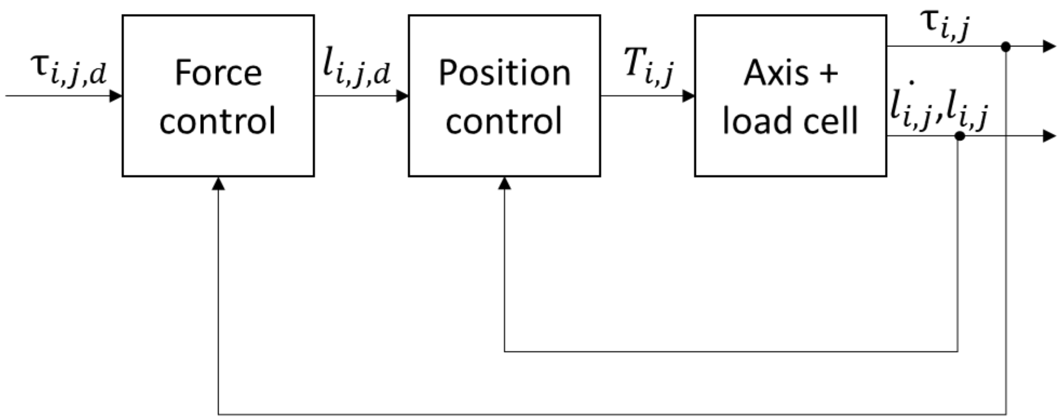

Fig. 7.2. Schematic of the force control loop with internal position control loop.

figure are represented only two of the six low level controllers), in parallel with a logic controller devoted to some procedures like homing and safety procedures. A higher level controller deals with the whole manipulator logic control and translates the user-imposed trajectories, defined using **p** and **R**, into joint-level reference trajectories. Some fixed trajectories are imposed to the mobile platform to validate the kinematic model: both the direct and inverse position control were tested.

The force control system is currently under development. Characterization of the friction model of the brushless motor and the electromechanical cylinder for the single actuator-load cell system was done. The force control loop will be based on the internal position control loop already implemented. Fig.7.2 shows the diagram of the force control: the input variable for the position control still remains the motor torque $T_{i,j}$. Zero force control logic for multi axes system will be developed later employing a decentralized architecture: the reference value of the forces is computed on a centralized unit relaying on relation (21).

Precision and accuracy tests are foreseen at a later stage.

BIBLIOGRAPHY

[1] Zavatsky, A., 1997, “A Kinematic-Freedom Analysis of a Flexed-Knee-Stance Testing Rig,” J. Biomech., 30(3), pp. 277–280.

[2] Varadarajan, K. M., Harry, R. E., Johnson, T., and Li, G., 2009, “Can In Vitro Systems Capture the Characteristic Differences Between the Flexion–Extension Kinematics of the Healthy and TKA Knee?” Med. Eng. Phys., 31(11), pp. 899–906.

[3] M. Forlani, N. Sancisi, M. Conconi, and V. Parenti-Castelli, ‘A new test rig for static and dynamic evaluation of knee motion based on a cable-driven parallel manipulator loading system’, Meccanica, vol. 51, no. 7, pp. 1571–1581, Jul. 2016.

[4] L. Luzi, N. Sancisi, M. Conconi, and V. Parenti-Castelli, ‘A New Test Rig for Human Joint and Prosthesis Characterization1’, J. Med. Devices, vol. 10, no. 2, pp. 020940-020940–3, May 2016.

[5] J.-P. Merlet, ‘Parallel manipulators: state of the art and perspectives’, in Robotics, Mechatronics and Manufacturing Systems, T. Takamori and K. Tsuchiya, Eds. Amsterdam: Elsevier, 1993, pp. 21–26.

[6] Dasgupta, B., Mruthyunjaya, T.S., 2000. The stewart platform manipulator: a review. Mech. Mach.Mach. Theory 35, 15-40.

[7] Gough, V. E. 1956. "Contribution to discussion to papers on research in tyre performance, by Cornell staff." Proc. Auto. Div. Instn. Mech. Engrs. 1956-57, 392.

[8] Stewart, D. A Platform with Six Degrees of Freedom. Proceedings of the Institution of Mechanical Engineers 180, 371–386 (1965).

[9] McCallion, H. & Truong, P. The analysis of a six-degree-of-freedom work station for mechanised assembly. in Proc. The Fifth Worm Congr. for the Theory of Machines and Mechanisms 611–616 (1979).

[10] K. H. Hunt, ‘Structural Kinematics of In-Parallel-Actuated Robot-Arms’, J. Mech., Trans., and Automation, vol. 105, no. 4, pp. 705–712, Dec. 1983.

[11] E. F. Fichter, ‘A Stewart Platform- Based Manipulator: General Theory and Practical Construction’, The International Journal of Robotics Research, vol. 5, no. 2, pp. 157–182, Jun. 1986.

[12] M. Raghavan, ‘The Stewart Platform of General Geometry Has 40 Configurations’, J. Mech. Des, vol. 115, no. 2, pp. 277–282, Jun. 1993.

[13] C. W. Wampler, ‘Forward displacement analysis of general six-in-parallel sps (Stewart) platform manipulators using soma coordinates’, Mechanism and Machine Theory, vol. 31, no. 3, pp. 331–337, Apr. 1996.

[14] M. L. Husty, ‘An algorithm for solving the direct kinematics of general Stewart-Gough platforms’, Mechanism and Machine Theory, vol. 31, no. 4, pp. 365–379, May 1996.

[15] P. Dietmaier, ‘The Stewart-Gough Platform of General Geometry can have 40 Real Postures’, in Advances in Robot Kinematics: Analysis and Control, Springer, Dordrecht, 1998, pp. 7–16.

[16] C. Innocenti and V. Parenti-Castelli., "Exhaustive Enumeration of Fully-Parallel Kinematic Chains", *ASME International Winter Annual Meeting*, Chicago, November 6-11, 1994, Chicago, USA, DSC-Vol.55-2, Dynamic System and Control, pp.1135-1141.

[17] C. Innocenti and V. Parenti-Castelli, ‘Analytical form solution of the direct kinematics of a 4–4 fully in-parallel actuated six degree-of-freedom mechanism’, in RoManSy 9, Springer, Berlin, Heidelberg, 1993, pp. 41–50.

[18] Arai, T., Tanikawa, T., Merlet, J.P. and T. Sendai 1996. "Development of a new parallel manipulator with fixed linear actuators." ASME Proceedings of the Japan/USA Symposium on Flexible Automation. VoL 1, 145-149.

[19] M. Honegger, A. Codourey, and E. Burdet, ‘Adaptive control of the Hexaglide, a 6 dof parallel manipulator’, in Proceedings of International Conference on Robotics and Automation, 1997, vol. 1, pp. 543–548 vol.1.

[20] Z. Ji and P. Song, ‘Design of a reconfigurable platform manipulator’, Journal of Robotic Systems, vol. 15, no. 6, pp. 341–346.

[21] F-200iB_series9_brochure.

[22] F-100 _brochure.

[23] Symétrie NOTUS hexapod brochure.

[24] H. A. Akeel, ‘Programmable positioner for the stress-free assembly of assemblies’, US6425177B1, 30-Jul-2002.

[25] T. M. Guess and A. Stylianou, "Simulation of anterior cruciate ligament deficiency in a musculoskeletal model with anatomical knees," The open biomedical engineering journal, vol. 6, pp. 23-32, 2012.

[26] H. Hirschfeld, M. Thorsteinsdottir, and E. Olsson, "Coordinated ground forces exerted by buttocks and feet are adequately programmed for weight transfer during sit-to-stand," Journal of neurophysiology, vol. 82, no. 6, pp. 3921-3029, 1999.

[27] Frank C. Anderson and Marcus G. Pandy, "Dynamic optimization of human walking," Journal of biomechanical engineering, vol. 123, no. 5, pp. 381-390, 2001.

[28] T. F. Besier, D. G. Lloyd, J. L. Cochrane, and T. R. Ackland, ‘External loading of the knee joint during running and cutting maneuvers’:, Medicine and Science in Sports and Exercise, pp. 1168–1175, Jul. 2001.

[29] E. Kristianslund, O. Faul, R. Bahr, G. Myklebust, and T. Krosshaug, ‘Sidestep cutting technique and knee abduction loading: implications for ACL prevention exercises’, British Journal of Sports Medicine, vol. 48, no. 9, pp. 779–783, May 2014.

[30] Tsai L.W., ‘Robot Analysis: The Mechanics of Serial and Parallel’, Wiley.

[31] E. F. Fichter, ‘A Stewart Platform- Based Manipulator: General Theory and Practical Construction’, The International Journal of Robotics Research, vol. 5, no. 2, pp. 157–182, Jun. 1986.

[32] Conti, J. P., Clinton, C. M., Zhang, G., and Wavering, A. J., “Dynamic Variation of the Workspace of an Octahedral Hexapod Machine Tool During Machining”, Technical Research Report 97-28, ISR, University of Maryland.

[33] O. Masory and Jian Wang, ‘Workspace evaluation of Stewart platforms’, Advanced Robotics, vol. 9, no. 4, pp. 443–461, Jan. 1994.

[34] Haug,. E. J., Luh, C. M., Adkins, F.A., and Wang, J. Y., “Numerical Algorithms for Mapping Boundaries of Manipulator Workspaces”, AMSE Journal of Mechanical Design, Vol. 118, pp. 228-234, June 1996.

[35] Litvin, F.L., 1980, “Application of Theorem of Implicit Function System Existence for Analysis and Synthesis of Linkages,” Mechanism and Machine Theory, Vol. 15, pp. 115-125.

[36] Tsai, Y.C., and Soni, A.H., 1981, “Accessible Region and Synthesis of Robot Arms,” Journal of Mechanical Design, Vol. 103, pp. 803-811.

[37] Yang, D.C.H., and Lee, T.W., 1983, “On the Workspace of Mechanical Manipulators,” Journal of Mechanisms, Transmissions, and Automation in Design, Vol. 105, pp. 62-69.

[38] Freudenstein, F., and Primrose, E.J., 1984, “On the Analysis and Synthesis of the Workspace of a Three-Link, Turning-Pair Connected Robot Arm,” Journal of Mechanisms, Transmissions, and Automation in Design, Vol. 106, pp. 365-370.

[39] Spanos, J., and Kohli, D., 1985, “Workspace Analysis of Regional Structures of Manipulators,” Journal of Mechanisms, Transmissions, and Automation in Design, Vol. 107, pp. 216-222.

[40] Gosselin, C. M., “Determination of the Workspace of 6-DOF Parallel Manipulators”, ASME Journal of Mechanical Design, Vol. 112, No. 3, pp. 331-336, September 1990.

[41] Merlet, J-P., “Manipulateurs parallèles, 5eme partie : Détermination de l’espace de travail à orientation constante”, Rapport de Recherche 1645, INRIA, March 1992.

[42] J.-P. Merlet, ‘Singular Configurations of Parallel Manipulators and Grassmann Geometry’, The International Journal of Robotics Research, vol. 8, no. 5, pp. 45–56, Oct. 1989.

[43] P. Ben-Horin and M. Shoham, ‘Singularity analysis of a class of parallel robots based on Grassmann–Cayley algebra’, Mechanism and Machine Theory, vol. 41, no. 8, pp. 958–970, Aug. 2006.

[44] P. Ben-Horin and M. Shoham, ‘Singularity condition of six-degree-of-freedom three-legged parallel robots based on grassmann-cayley algebra’, IEEE Transactions on Robotics, vol. 22, no. 4, pp. 577–590, Aug. 2006.

[45] Hao, F. & McCarthy, J. M. (1998). Conditions for Line-Based Singularities in Spatial Platform Manipulator, Journal of Robotic Systems, 15(1), pp. 43-55, 1998.

APPENDIX A.1 – PARKER ELECTROCYLINDER ACTUATOR SPECIFICATION

Cylinder size type	Unit	ETH032			ETH050			ETH080		
		M05	M10	M16[4]	M05	M10	M20[4]	M05	M10	M32[4]
Screw lead	[mm]	5	10	16	5	10	20	5	10	32
Screw diameter	[mm]		16			20			32	
Travels, speeds and accelerations										
Available strokes [1) 2)]	[mm]	continuous from 50-1000 & standard strokes			continuous from 50-1200 & standard strokes			continuous from 50-1600 & standard strokes		
Max. permissible speed at stroke =										
50-400 mm	[mm/s]	333	667	1067	333	667	1333	267	533	1707
600 mm	[mm/s]	286	540	855	333	666	1318	267	533	1707
800 mm	[mm/s]	196	373	592	238	462	917	267	533	1707
1000 mm	[mm/s]	146	277	440	177	345	684	264	501	1561
1200 mm	[mm/s]	-	-	-	139	270	536	207	394	1233
1400 mm	[mm/s]	-	-	-	-	-	-	168	320	1006
1600 mm	[mm/s]	-	-	-	-	-	-	140	267	841
Max. Acceleration	[m/s²]	4	8	12	4	8	15	4	8	15
Forces										
Max. axial traction/thrust force motor inline	[N]	3600	3700	2400	9300	7000	4400	17800	25100	10600
Max. axial traction/thrust force [3] Motor parallel	[N]		3280	2050		4920	2460		11620	3630
Equivalent dynamic axial force at a lifetime of 2500 km	[N]	1130	1700	1610	2910	3250	2740	3140	7500	6050
Max. transmissible torque / force constant										
Max. transmissible torque inline motor	[Nm]	3.2	6.5	6.8	8.2	12.4	15.6	15.7	44.4	60.0
Max. transmissible torque [3] Motor parallel	[Nm]	3.5	6.4		9.1	9.3		17.5	22.8	
Force constant motor inline [5]	[N/Nm]	1131	565	353	1131	565	283	1131	565	177
Force constant motor parallel [5]	[N/Nm]	1018	509	318	1018	509	254	1018	509	159
Weight [6]										
Weight of base unit with zero stroke (incl. piston rod)	[kg]	1.2	1.2	1.4	2.2	2.2	2.4	7.1	7.5	8.5
Additional weight of inline unit	[kg]		0.7			1.0			3.2	
Additional weight of parallel unit	[kg]		0.8			1.0			3.1	
Mass of additional stroke (incl. piston rod)	[kg/m]		4.5			8.2			18.2	
Weight of piston rod with zero stroke	[kg]		0.06			0.15			0.59	
Weight of piston rod - additional length	[kg/m]		0.99			1.85			4.93	
Mass moments of inertia										
Motor parallel without stroke	[kgmm²]	8.3	8.8	14.1	30.3	30.6	38.0	215.2	213.6	301.9
Motor inline without stroke	[kgmm²]	7.1	7.6	12.9	25.3	25.7	33.1	166.2	164.5	252.9
Parallel/inline motor per meter	[kgmm²/m]	41.3	37.6	41.5	97.7	92.4	106.4	527.7	470.0	585.4
Accuracy: Bidirectional Repeatability (ISO230-2)										
Motor inline	[mm]					±0.03				
Motor parallel	[mm]					±0.05				
Efficiency										
Motor inline (the efficiency includes all friction torques)	[%]					90				
Motor parallel (the efficiency includes all friction torques)	[%]					81				
Ambient conditions										
Operating Temperature	[°C]					-10...+70				
Ambient temperature	[°C]					-10...+40				
Storage temperature	[°C]					-20...+40				
Humidity	[%]					0...95 % (non-condensing)				
Location height range	[m]					max. 3000				

Fig. A.1.1. Parker electro-cylinder actuator specification.

APPENDIX A.2 – HBM LOAD CELL SPECIFICATION

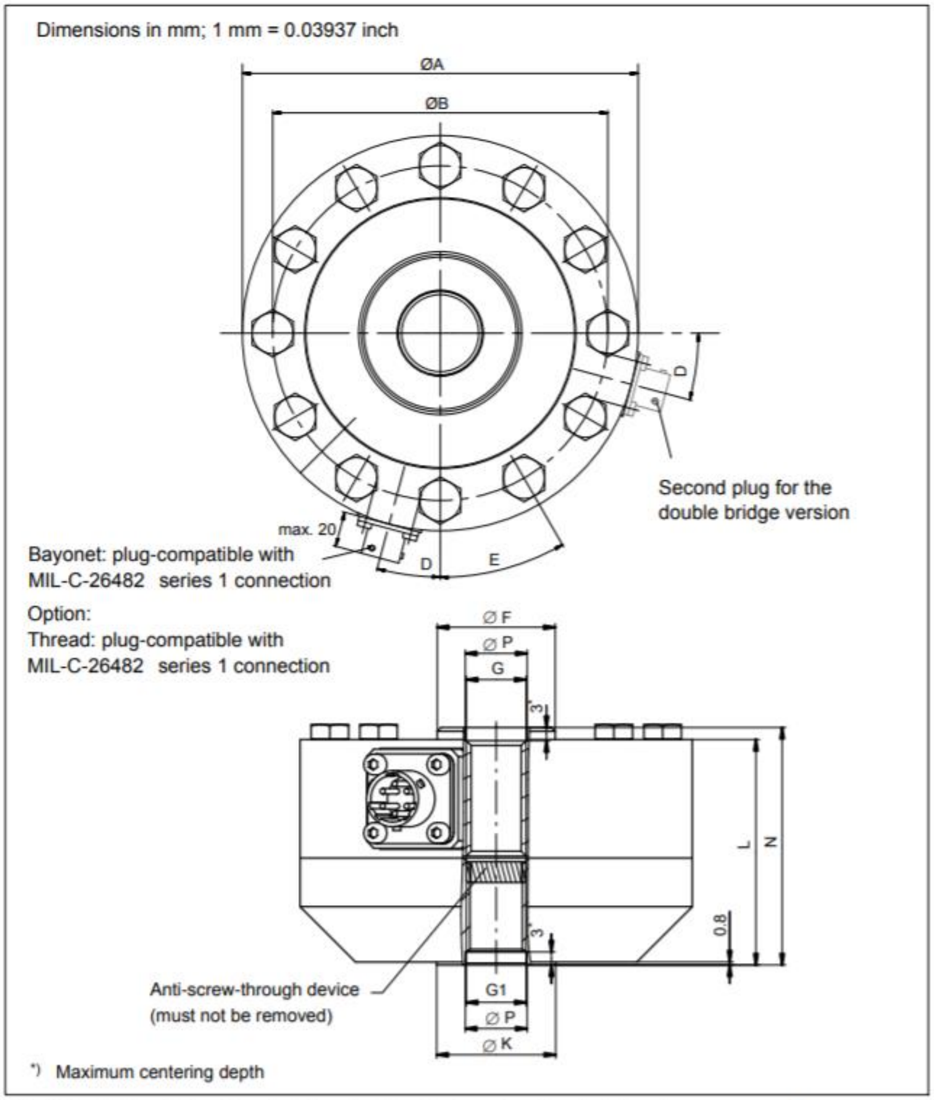

Nominal (rated) force	Dimensions in	ØA	ØB	D	E	ØF	G
1.25 kN - 5 kN	mm	104.8	88.9	22.5°	45°	30.4	M16x2-4H 28.4 mm deep
	inch	4.13	3.5			1.2	
12.5 kN - 25 kN	mm	104.8	88.9	22.5°	45°	31.5	M16x2-4H 28.4 mm deep
	inch	4.13	3.5			1.24	
50 kN	mm	153.9	130.3	15°	30°	61.2	M33x2-4H 35.6 mm deep
	inch	6.06	5.13			2.41	
125 kN	mm	153.9	130.3	15°	30°	67.3	M33x2-4H 35.6 mm deep
	inch	6.06	5.13			2.65	

Nominal (rated) force	Dimensions in	G1	ØK	L	N	$ØP_{H8}$
1.25 kN - 25 kN	mm	M16x2-4H 22.1 mm deep	31.8	60.3	63.5	16.5
	inch		1.25	2.37	2.5	0.65
50 kN - 125 kN	mm	M33x2-4H 35.6 mm deep	57.2	85.9	89	33.5
	inch		2.25	3.38	3.5	1.32
250 kN	mm	M42x2-4H 54.6 mm deep	76.2	108	114.3	43
	inch		3	4.25	4.5	1.69
500 kN	mm	M42x2-4H 82.6 mm deep	114	152.4	165.1	73
	inch		4.49	6	6.5	2.87

Fig. A.2.1. HBM load cell specification.

Nominal (rated) force	F_{nom}	kN	1.25	2.5	5	12.5	25	50	125	250	500
Nominal (rated) sensitivity	C_{nom}	mV/V	1 ... 1.5 [1]			2 ... 2.5 [1]					
Accuracy class			0.03			0.04			0.05		0.06
Relative repeatability error in an unmodified mounting position	b_{rg}	%	0.025								
Relative zero signal error	$d_{s,0}$	%	1								
Relative reversibility error [2] (at $0.4 \cdot F_{nom}$)	$v_{0.4}$	%vl %vc	< 0.075 0.03			< 0.1 0.04		< 0.125 0.05			< 0.125 0.05
Relative linearity error	d_{lin}	%	< ±0.03			< ±0.04					< ±0.06
Relative creep over 30min	d_{crf+E}	%	< ±0.04			< ±0.025					
Effect of temperature on sensitivity/10K	TK_C	%	< ±0.015								
Temperature effect on the zero signal/10K	TK_0	%	< ±0.015								
Bending moment influence (at $10\% \cdot F_{nom} \cdot 10$ mm)	d_Q	%	< 0.01								
Output resistance	R_o	Ω	280 ... 360								
Input resistance	R_i	Ω	> 345								
Insulation resistance	R_{is}	GΩ	> 2								
Reference excitation voltage	U_{ref}	V	5								
Operating range of excitation voltage	$B_{U,G}$	V	0.5 to 12								
Reference temperature	T_{ref}	°C [°F]	+23 [73.4]								
Nominal (rated) temperature range	$B_{T,nom}$	°C [°F]	-10 ... +45 [+14 ... +113]								
Operating temperature range	$B_{T,G}$	°C [°F]	-30 ... +85 [-22 ... +185]								
Storage temperature range	$B_{T,S}$	°C [°F]	-30 ... +85 [-22 ... +185]								
Max. operating force	(F_G)	% v. F_{nom}	240								
Breaking force	(F_B)	% v. F_{nom}	> 400								
Static lateral limit force [3]	(F_Q)	% v. F_{nom}	100								
Bending limit moment	$M_{b\ perm}$	N·m	30	60	125	315	635	1270	3175	5715	11430
Limit torque	M_L	N·m	30	60	125	315	635 [4]	1270	3175	5715	11430
Nominal (rated) displacement	s_{nom}	mm	0.02			0.03			0.04	0.05	0.06
Fundamental resonance frequency	f_G	kHz	4.5	5.9	9.3	6.6	9.2	6.5	8.1	6.6	6.1
Rigidity	F/S	10^5 N/mm	0.625	1.25	2.5	4.17	8.33	16.7	31.3	50.0	83.3
Permissible vibrational stress (Vibration bandwidth per DIN 50100)	F_{rb}	% v. F_{nom}	200								
Weight (without cable) With adapter Without adapter		kg lbs kg lbs	1.2 2.65 0.5 1.1			3 6.61 1.3 2.87		10 22.05 5 11.02		23 50.71 11 24.25	60 132.28 28 61.73
Immunity from interference (EN 61326-1, Table A.1)			Industrial environment								
Electromagnetic field (AM)		V/m	10								
Magnetic field		A/m	30								
Electrostatic discharge (ESD)											
Contact discharge		kV	4								
Air discharge		kV	8								
Burst (rapid transients)		kV	1								
Surge (impulse voltages)		kV	1								
Grid-bound interferences (AM)		V	3								

Fig. A.2.2. HBM load cell specification.

APPENDIX A.3 – SINGULAR SURFACES

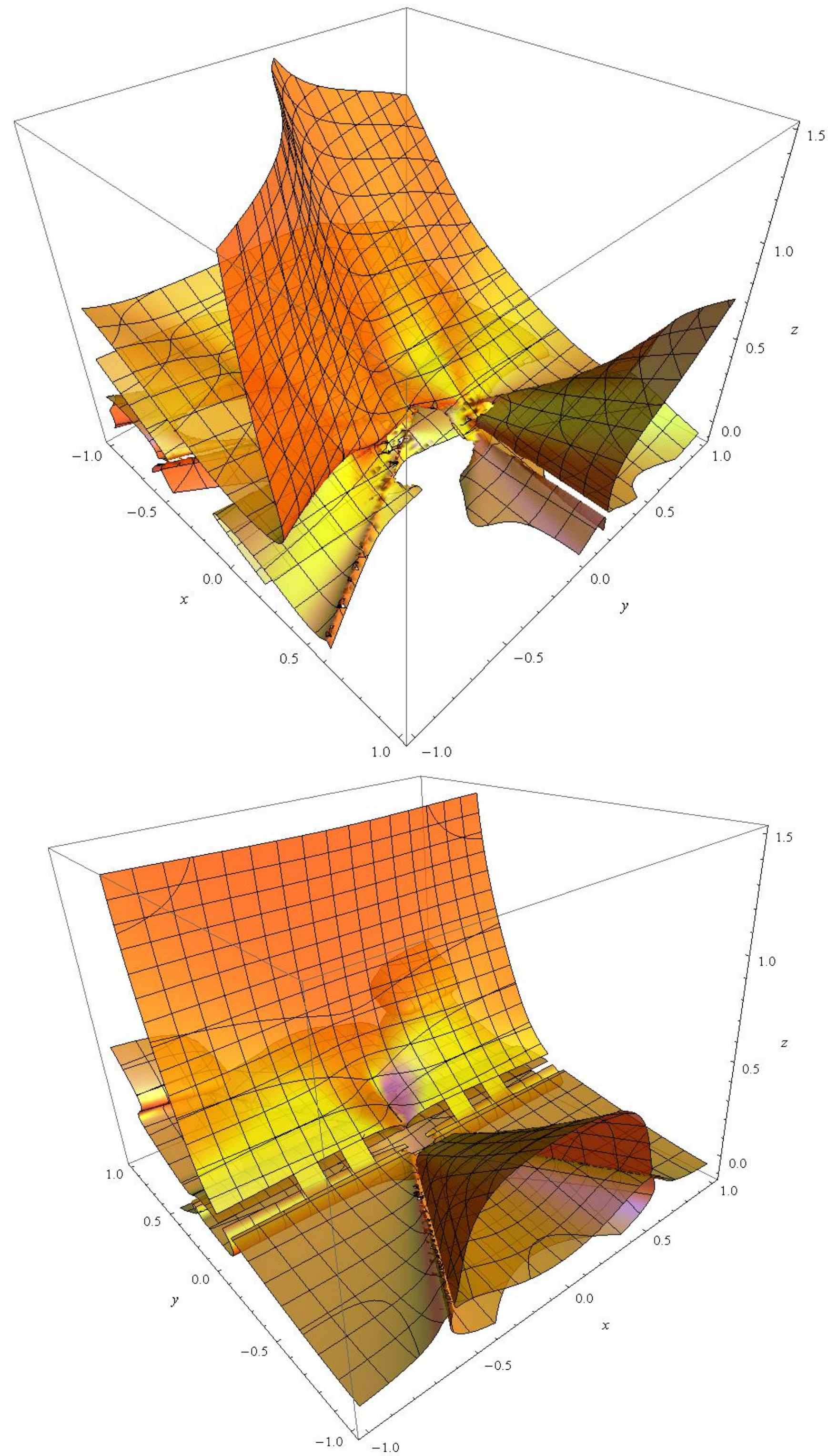

Fig. A.3.2. Fixed orientation singular surface with η =3 0°, φ = 0° and ψ = 0° (top); fixed orientation singular surface with η = 0°, φ = 0° and ψ = 30° (bottom).

APPENDIX A.4 – CONSTRUCTIVE DETAILS OF THE MANIPULATOR

Figure A.4.1. Details of the constructive solutions adopted to reach the required mobility

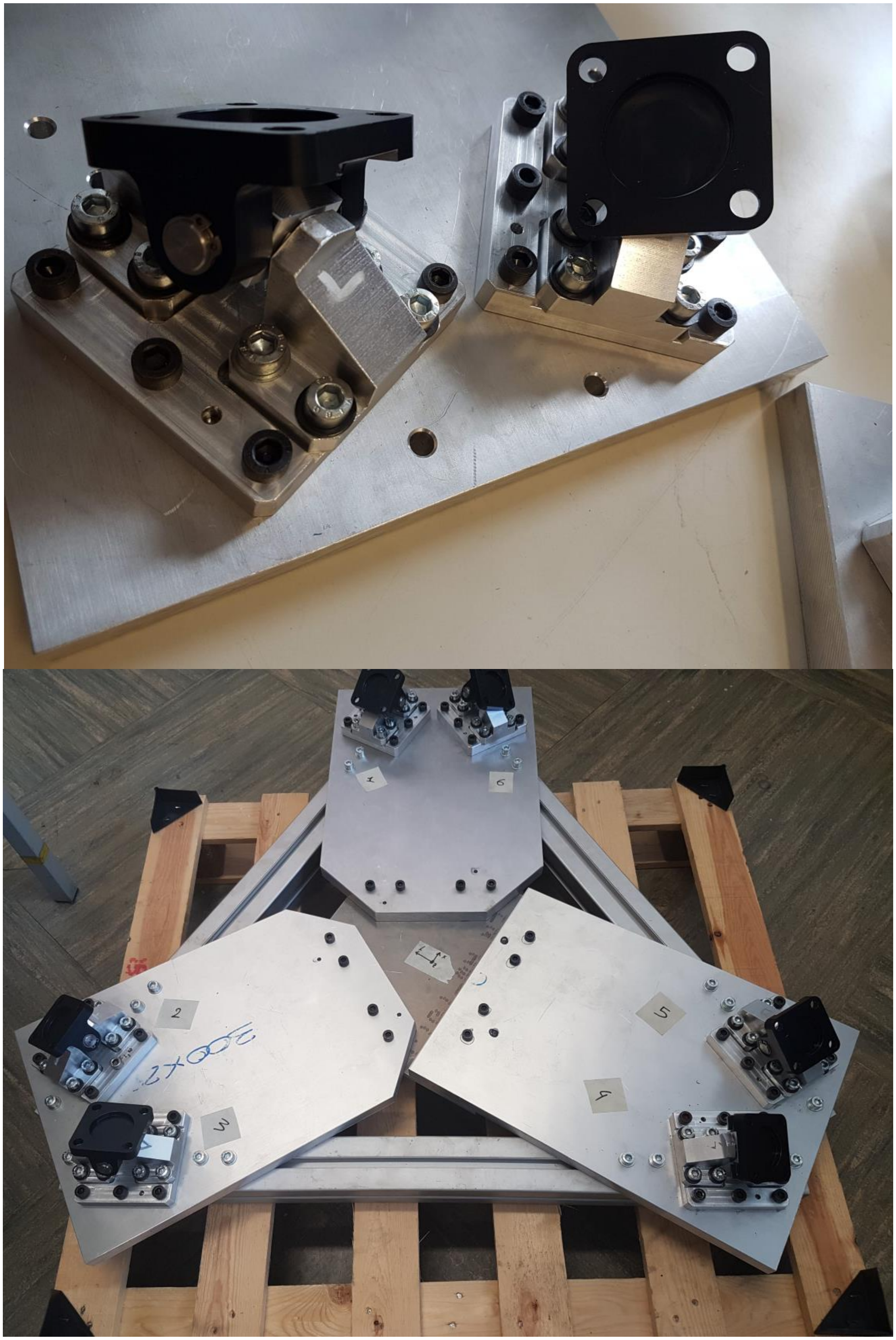

Figure A.4.2. Details of the constructive solutions adopted no the fixed base.